This article has been accepted for inclusion in a future issue of this journal. Content is final as presented, with the exception of pagination.

Assessment and Combination of SMAP and Sentinel-1A/B-Derived Soil Moisture Estimates With Land Surface Model Outputs in the Mid-Atlantic Coastal Plain, USA

Hyunglok Kim, Sangchul Lee, Michael H. Cosh, *Senior Member, IEEE*, Venkataraman Lakshmi, Yonghwan Kwon, and Gregory W. McCarty

***Abstract*— Prediction of large-scale water-related natural disasters such as droughts, floods, wildfires, landslides, and dust outbreaks can benefit from the high spatial resolution soil moisture (SM) data of satellite and modeled products because antecedent SM conditions in the topsoil layer govern the partitioning of precipitation into infiltration and runoff. SM data retrieved from Soil Moisture Active Passive (SMAP) have proved to be an effective method of monitoring SM content at different spatial resolutions: 1) radiometer-based product gridded at 36 km; 2) radiometer-only enhanced posting product gridded at 9 km; and 3) SMAP/Sentinel-1A/B products at 3 and 1 km. In this article, we focused on 9-, 3-, and 1-km SM products: three products were validated against *in situ* data using conventional and triple collocation analysis (TCA) statistics and were then merged with a Noah-Multiparameterization version-3.6 (NoahMP36) land surface model (LSM). An exponential filter and a cumulative density function (CDF) were applied for further evaluation of the three SM products, and the maximize-*R* method was applied to combine SMAP and NoahMP36 SM data. CDF-matched 9-, 3-, and 1-km SMAP SM data showed reliable performance: *R* and ubRMSD values of the CDF-matched SMAP products were 0.658, 0.626, and 0.570 and 0.049, 0.053, and 0.055 m^3/m^3, respectively. When SMAP and NoahMP36 were combined, the *R*-values for the 9-, 3-, and 1-km SMAP SM data were greatly improved: *R*-values were 0.825, 0.804, and 0.795, and ubRMSDs were 0.034, 0.036, and 0.037 m^3/m^3, respectively. These results indicate the potential uses of SMAP/Sentinel data for improving regional-scale SM estimates and for creating further applications of LSMs with improved accuracy.**

***Index Terms*— Data combination, data validation, land surface model, microwave remote sensing, Sentinel-1A/B, soil moisture (SM), Soil Moisture Active Passive (SMAP).**

Manuscript received August 9, 2019; revised February 19, 2020 and April 18, 2020; accepted April 19, 2020. This work was supported in part by the U.S. Department of Agriculture (USDA) Natural Resources Conservation Service (NRCS) in association with the Wetland Component of the National Conservation Effects Assessment Project (CEAP), in part by the USDA—National Institute of Food and Agriculture (NIFA) under Grant 2017-67003-26484 and Grant 2017-67003-26485, in part by the NASA Terrestrial Ecology Program under Grant NNX17AE66G, and in part by the NASA Terrestrial Hydrology Program through the Program Manager Jared Entin under Grant NNX12AP75G. The work of Hyunglok Kim was supported in part by the Future Investigators in NASA Earth and Space Science and Technology (FINESST) Award under Award #80NSSC19K1337 and in part by the Bicentennial Fellow Scholarship from the Department of Engineering Systems and Environment, University of Virginia. *(Corresponding author: Sangchul Lee.)*

Hyunglok Kim and Venkataraman Lakshmi are with the Department of Engineering Systems and Environment, University of Virginia, Charlottesville, VA 22904 USA (e-mail: hk5kp@virginia.edu; vlakshmi@virginia.edu).

Sangchul Lee is with the Department of Environmental Science and Technology, University of Maryland, College Park, MD 20742 USA, and also with Hydrology and Remote Sensing Laboratory, U.S. Department of Agriculture—Agricultural Research Service, Beltsville, MD 20705 USA (e-mail: sangchul.lee84@gmail.com).

Michael H. Cosh and Gregory W. McCarty are with Hydrology and Remote Sensing Laboratory, U.S. Department of Agriculture—Agricultural Research Service, Beltsville, MD 20705 USA (e-mail: michael.cosh@ars.usda.gov).

Yonghwan Kwon is with Hydrological Sciences Laboratory, NASA Goddard Space Flight Center, Greenbelt, MD 20771 USA, and also with Earth System Science Interdisciplinary Center, University of Maryland, College Park, MD 20742 USA (e-mail: yhkwon@umd.edu).

Color versions of one or more of the figures in this article are available online at http://ieeexplore.ieee.org.

Digital Object Identifier 10.1109/TGRS.2020.2991665

I. Introduction

SOIL moisture (SM) is a key indicator of both landscape hydrologic and biogeochemical processes [1]–[3]. The amount of water stored in the topsoil layer is generally determined through interaction among hydrologic components precipitation, evapotranspiration (ET), surface runoff, percolation, groundwater recharge, and plant uptake [1], along with the effect of soil physical characteristics (e.g., hydraulic conductivity). Aside from hydrology, SM also allows estimation of biogeochemical fluxes and storage (e.g., nutrient reduction and transport and carbon storage) due to linkage of these processes to SM [2]. SM is also used to predict the effect of human activities on agriculture management because soil–water deficiency is a driving factor that determines irrigation practices to curb crop water stress [4]. Hence, spatial and temporal variations in SM offer important signals for understanding hydrologic and biogeochemical processes and patterns.

Consistent and routine monitoring of every location on Earth can be accomplished with satellite remote sensing [5]. It is a known fact that SM contents retrieved from satellite microwave instruments provide an effective way to monitor SM variability with near-daily temporal resolution [6]–[8], and various methods for estimating SM data from satellite microwave instruments have been proposed [9], including the Advanced Microwave Scanning Radiometer (AMSR-E), the Advanced Scatterometer (ASCAT), the Soil Moisture and

0196-2892 © 2020 IEEE. Personal use is permitted, but republication/redistribution requires IEEE permission.
See https://www.ieee.org/publications/rights/index.html for more information.

Authorized licensed use limited to: University of Virginia Libraries. Downloaded on June 11,2020 at 17:07:51 UTC from IEEE Xplore. Restrictions apply.

This article has been accepted for inclusion in a future issue of this journal. Content is final as presented, with the exception of pagination.

Ocean Salinity (SMOS), the Advanced Microwave Scanning Radiometer 2 (AMSR2), and the Soil Moisture Active Passive (SMAP) [10]–[14]. Researchers have also experimented with applying Global Navigation Satellite System (GNSS) signals to determine surface SM. This passive bistatic radar technique shows the possibility that reflected GNSS signals from Earth's surface might be used to describe Earth's surface properties [15]. It has been proven that satellite-based SM estimates are capable of providing regional- and global-scale SM estimates for use in modeling the interactions between land and atmosphere, helping us to provide high-accuracy, near-real-time climate forecasting [16], [17]. SM estimates from remote sensing technique are also recognized as a promising means of providing large-scale SM information because the spatial range has fewer constraints [10]. Furthermore, various studies using satellite SM data have consistently progressed in terms of applications such as drought monitoring [18], irrigation detection [4], [19], runoff modeling [20], flood forecasting [21], and many other areas [22].

However, most microwave-band radiometry-based SM retrievals from space provide SM estimates at 10 to 36 km resolution globally [8], [10]: the spatial resolution of SM estimates from sun-synchronous satellite microwave systems are restricted by the diameter required by the antenna which produces the long wavelengths (i.e., L-, C-, and X-bands) necessary in estimating SM data. Despite the high sensitivity of microwave radiometers to SM variability, their spatial resolution remains coarser than that of active microwave and optical systems. However, high-resolution surface SM contents derived from various satellite sensors are required for a wide range of operational applications, including irrigation management, agricultural activities, and hydrological modeling.

Researchers have proposed various methods of improving the spatial resolution of microwave-based SM estimates through synergistic use of other satellite and model products [8], [23]–[29]. These previous studies developed disaggregation methods and compared the performances of downscaled SM products retrieved from different microwave sensors such as AMSR2 onboard GCOM-W1, Microwave Imaging Radiometer using Aperture Synthesis (MIRAS) onboard SMOS, and the radiometer onboard SMAP. SM estimates (or bright temperature values) from these sensors are then disaggregated into finer spatial resolutions using auxiliary information obtained from Moderate Resolution Imaging Spectroradiometer (MODIS) onboard the Earth Observing System (EOS) Terra and Aqua platforms, Synthetic-Aperture Radar (SAR) onboard Sentinel-1, Landsat satellites, and so on. In particular, NASA's SMAP mission has been implemented to provide not only the 36- and 9-km grid sizes of SM data from L-band radiometer brightness temperature (T_B) but also the 3- and 1-km SM data from a combination of SMAP and Sentinel-1A/B observations. These gridded data of SM with 3 and 1 km were produced by combining the Sentinel-1A/B C-band radar backscatter (σ^0) and SMAP radiometer T_B observations. This newly available SM product with 1-km resolution from SMAP and Sentinel-1A/B observations would be highly beneficial to operational applications such as water resource and irrigation management, hydrological modeling, watershed management, and many other surface processes [30]. However, before practical use of these high-resolution SMAP data sets can begin, it will be necessary to validate the data [31]. These downscaled products have yet to be thoroughly validated against ground observations. They have not been fully investigated with regard to their effectiveness in improving SM data quality when used with modeled SM products.

The objective of this article is to explore the accuracy of three SM data sets from SMAP—9, 3, and 1 km—and the appropriateness of these high spatial resolution SM data for synergistic use with modeled SM products. We validated newly released SMAP Enhanced (9 km) and SMAP/Sentinel-1 (3 and 1 km) products against ground-based measurements located in an agricultural landscape within the Mid-Atlantic Coastal Plain, USA. By doing so, we provide new insights into the applicability of high-resolution SM products from SMAP/Sentinel-1A/B observations. Specifically, we have highlighted the advantages and limitations of the newly available high spatial resolution SMAP products for various hydrological and agricultural applications, thus helping watershed scientists and conservationists to efficiently monitor hydrologic processes and develop water management plans.

II. Study Area

The study domain was the upper portion of the Choptank River watershed (CRW, approximately 1,756 km^2) along the Eastern shore of Maryland within the Mid-Atlantic Coastal Plain, USA (Fig. 1). The CRW is recognized as an "impaired" water body under Section 303 (d) of the Clean Water Act owing to excessive loadings of sediment and nutrients from croplands [32]. As a benchmark watershed, the CRW has been extensively monitored and studied by the USDA Agricultural Research Service (ARS) in the Conservation Effects Assessment Project (CEAP) [33] as well as within the Long-term Agroecosystem Research (LTAR) Network [34]. This area is characterized by low topographic relief and a temperate, humid climate with an annual average precipitation of 1,200 mm [35]. Precipitation is fairly uniform over the course of the year, while ET differs seasonally (e.g., low and high during winter and summer seasons, respectively), leading to a high seasonality of overall water balance [36]. According to the Multi-Resolution Land Characteristics (MRLC) Consortium National Land Cover Database (NLCD) for the year 2016, the land use of the study domain is dominated by croplands used mainly for corn and soybeans, followed by forest, developed lands, pasture, and open water (Fig. 1 and Table VIII in Appendix A). The U.S. Soil Survey Geographical Database (SSURGO) indicates a large portion (60%) of soils within the domain is well- or moderately well-drained, and the remainder is moderately poorly drained (Table VIII and Fig. 7 in Appendix A).

III. Data Description

A. SMAP and SMAP/Sentinel-1A/B Soil Moisture Products

The 3- and 1-km spatial resolutions of SMAP/Sentinel-1A/B SM data were derived using σ^0 from the Sentinel-1A/B and T_B from the 9-km enhanced radiometer data because

Authorized licensed use limited to: University of Virginia Libraries. Downloaded on June 11,2020 at 17:07:51 UTC from IEEE Xplore. Restrictions apply.

This article has been accepted for inclusion in a future issue of this journal. Content is final as presented, with the exception of pagination.

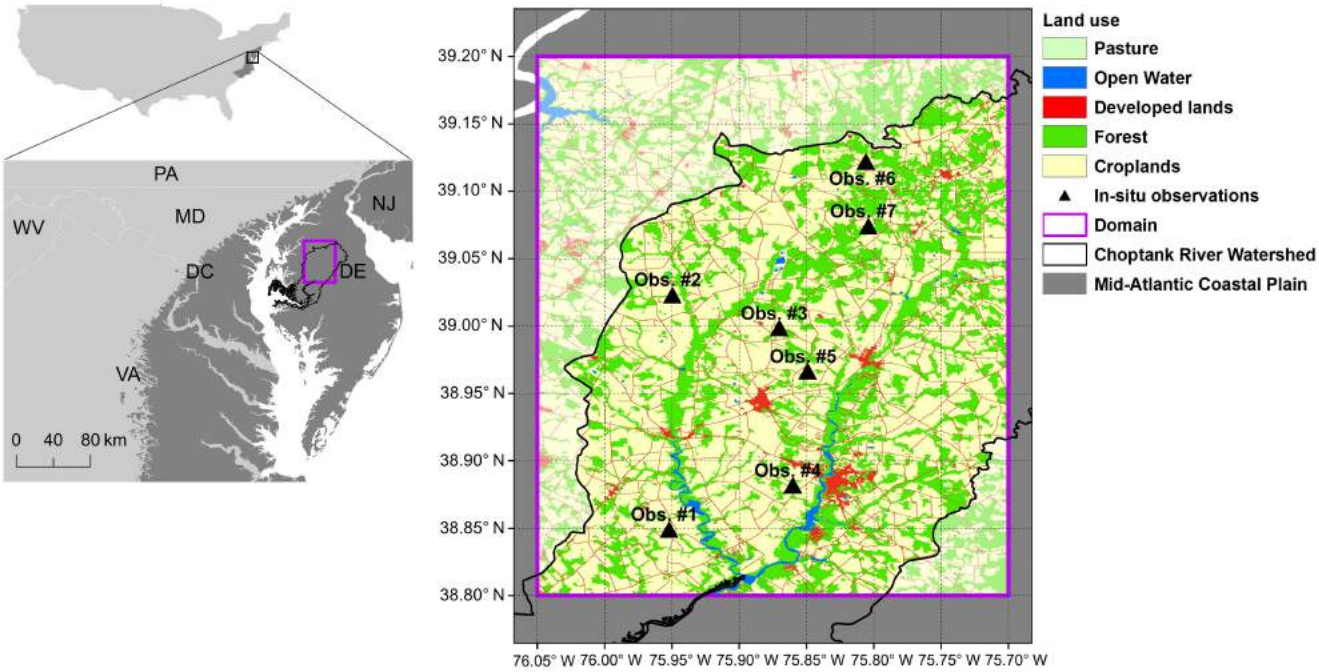

Fig. 1. Location of the study domain. Note: The 15 NLCD land use classes were aggregated into five classes according to their similarity (Table IX in Appendix A).

Sentinel C-band SAR observations have much higher resolution (∼50 m) than SMAP radiometer observations [37]. Sentinel-1 is a satellite constellation managed by the European Space Agency; composed of a constellation of two satellites, Sentinel-1A and Sentinel-1B, which share the same orbital plane. The constellation is in a sun-synchronous, near-polar orbit with a 12-day repeat cycle, and it completes 175 orbits per cycle [38]. Sentinel-1A/B carries a C-band SAR instrument (central frequency at 5.405 GHz) which provides σ^0 data available in all weather conditions, day or night. The SMAP/Sentinel-1 L2 SM product uses Sentinel-1A/B C-band SAR σ^0 measurements to disaggregate the SMAP L-band T_B measurements from the ∼9- to 3-km and 1-km EASE2-grid projection. To reduce the speckle of ∼50-m resolution of SAR observations and the corresponding swath of up to 400 km, the SAR observations were aggregated to a resolution of 1 km before disaggregation was performed. For this reason, the finest spatial resolution of SMAP/Sentinel-1 SM product is 1 km [30]. The L2_SM_SP product, 3- and 1-km SMAP/Sentinel-1 SM data were generated from the SMAP/Sentinel Active–Passive algorithm introduced in [39], which was updated based on a snapshot retrieval approach [40], [41]. In this article, we obtained SMAP/Sentinel-1 3- and 1-km data through NSIDC (https://nsidc.org/data/spl2smap_s). Refer to [39] for further details about SMAP/Sentinel SM product.

This article used the 9-km enhanced SMAP SM (hereafter, SMAP-9 km) and the 3- and 1-km SMAP-Sentinel SM (hereafter, SMAP/Sentinel-3 km and SMAP/Sentinel-1 km, respectively). The temporal resolution of SMAP/Sentinel SM data depends greatly on the number of C-band SAR acquisition from Sentinel-1A and -1B because the spatial coverage and revisit interval of the Sentinel-1A and -1B cannot be matched to the SMAP observations. Consequently, the temporal resolution of SMAP/Sentinel SM is about 8 days. In this article, the temporal coverage was from December 2016 to October 2018.

B. Land Surface Model

Various land surface models (LSMs), such as Mosaic [42], Variable Infiltration Capacity (VIC) [43], Catchment LSM-Fortuna 2.5 (CLSM F2.5) [44], Noah [45], and Noah with Multiparameterization options (Noah-MP) [46], [47], have been widely used to predict surface to root-zone SM [1], [48]–[50]. Among the existing LSMs, in this article, we used Noah-MP version 3.6 (hereafter, NoahMP36), implemented in the NASA Land Information System (LIS) [51], [52], to generate SM outputs similar to previous research [53]. Compared with previous Noah-3.6 LSMs, NoahMP36 has been improved in several aspects of hydrological processes, including snow physics [54], and warm season processes [53], [55]. Noah-MP LSM uses multiple options for important land–atmosphere interaction processes, and it contains a separate vegetation canopy defined by a canopy top and bottom; crown radius; and leaves with described dimensions, orientation, density, and radiometric properties [46]. To precisely estimate surface energy and the water transfer process, the canopy uses a two-stream radiation transfer approach with shading effects [56], [57]. Noah-MP has also made several improvements in estimating different hydrological variables, including multilayer snow variables, surface water infiltration, runoff, vegetation groundwater transfer, and storage. Refer to [57]–[59] for further detailed

Authorized licensed use limited to: University of Virginia Libraries. Downloaded on June 11,2020 at 17:07:51 UTC from IEEE Xplore. Restrictions apply.

This article has been accepted for inclusion in a future issue of this journal. Content is final as presented, with the exception of pagination.

information. Hourly NoahMP36 surface (0–10 cm soil depth) SM data (hereafter, SM_{MOD}) with the 9-, 3-, and 1-km spatial resolution were produced to match the temporal and spatial resolutions of SMAP or SMAP/Sentinel SM data sets. NoahMP36 was driven by the North American Land Data Assimilation System project phase 2 (NLDAS-2) [60] meteorological forcing data during 2006–2018. We then used the SM data from 2016 to 2018 which corresponded to the SMAP and SMAP/Sentinel SM products. These modeled products were used as one half of the parent data designated for combination with SMAP or SMAP/Sentinel SM data (Section IV-E) and one component of the triplet used for the triple collocation analysis (TCA) (Section IV-C).

C. Ground Observation

In situ SM measurements have served an essential role in validating modeled and remotely sensed SM retrievals [61], [62]. The SMAP and SMAP/Sentinel SM products were validated using hourly SM (m^3/m^3) measured at depths of 5 cm below the land surface using the Stevens Water Hydra Probes SM sensor. Hourly rainfall data were also collected at each station by Texas Electronics 525 tipping bucket rain gauges [63]. These sensors were located in the vicinity of cropland boundaries in grasslands or short-maintained lawns (Fig. 1). The seven observation locations, surface SM, climatic variables (i.e., surface temperature and precipitation), vegetation, and other land property information are included in Table I. The majority filter was used to calculate major land cover types (eighth row in Table I) for different pixel resolutions.

In this article, soil properties are derived from the USDA Natural Resources Conservation Service (NRCS) Soil Survey Geographic Database (SSURGO; https://websoilsurvey.nrcs.usda.gov/). This database provides nationwide information on detailed soil characteristics; thus, it has been widely used as ancillary data for hydrology [64], ecology [65], and biogeochemistry [66].

D. Other Data Sets

To further investigate the impact of hydrological variables on SM estimates from SMAP and SMAP/Sentinel-1A/B, we used vegetation, precipitation, and land cover properties. For precipitation, we used the Global Precipitation Measurement (GPM) constellation (Section III-D.2, Fig. 2), the vegetation index from the MODIS Normalized Difference Vegetation Index (NDVI) (Section III-D.1, Fig. 2), and the land's heterogeneity indicator from the Gini–Simpson Index calculated from a land use map from MRLC NLCD (Section III-D.2, Fig. 2).

1) Normalized Difference Vegetation Index (NDVI): The NDVI was obtained from the MODIS Aqua satellite (MYD13A2), which provides global NDVI data every 16 days as a gridded level-3 product with a spatial resolution of 1 km. NDVI is the most commonly used vegetation index for analyzing the status of vegetation growth and it represents the vegetation density and chlorophyll content of vegetation [67], [68]. MODIS is onboard two NASA satellites Terra and Aqua, which were launched on December 1999 and May 2002, respectively. Details of the MODIS land data are available at the MODIS website (https://modis.gsfc.nasa.gov) [67].

2) Global Precipitation Measurement and Land Cover Data: Launched on February 20, 2014, by NASA and JAXA, GPM is an international satellite mission intended to provide precipitation and snowfall on a global scale every 30 min [69]. There are many products available from the GPM Core Observatory; of relevance to our present work are those associated with a high-quality, late-run GPM Core Observatory product used in producing the Integrated Multi-satellitE Retrievals (IMERG) at a temporal scale of every 30 min with 0.1° grid boxes. In this article, we used GPM IMERG Final precipitation L3 half-hourly data.

The Gini–Simpson Index [70] was calculated using MRLC NLCD (https://www.mrlc.gov/) to provide information on the heterogeneity over the study areas. The NLCD provides national-scale land cover classification with a medium resolution (30 m) for national applications [71]. The latest version (2016 land cover map) used in this article was developed to support monitoring land cover change and environmental models by offering a nationwide consistent multitemporal land cover and land cover change database [71].

IV. Methodology and Data Preparation

Accuracy of the SMAP and SMAP/Sentinel SM data sets was evaluated against the seven ground observations shown in Fig. 1 using four statistical indicators (Section IV-A). To overcome the sensing depth mismatch between satellite and ground observations, we considered an exponential filter (Section IV-B). The TCA was adopted to innate errors in SMAP, SMAP/Sentinel, and observation SM data (Section IV-C). In addition, a cumulative density function (CDF) matching method was applied to SMAP-9 km and SMAP/Sentinel-3- and -1-km data sets (Section IV-D), and then the usability and effectiveness of downscaled SMAP and SMAP/Sentinel SM products were examined along with the NoahMP36 SM data (Section IV-E). Finally, Taylor diagrams were included to effectively show comparative results of different SM products, including satellite, model, and combined SM data sets (Section IV-F).

A. Statistic Metrics for the Validation of SM Data

In this article, four conventional statistical indicators were used including Pearson's correlation coefficient (hereafter, R), bias, root-mean-square difference (RMSD), and unbiased RMSD (ubRMSD) that are calculated using the equations shown in [72] with p-value less than 0.05. We only considered data points where all the data, 9-, 3-, and 1-km SM products, were available simultaneously. Hereafter, we used SM_{REF} for SM data from *in situ* (reference SM), SM_{MOD} for SM data from NoahMP36 data (model-based SM), and SM_{SAT} for SMAP SM data (satellite-based SM).

B. Exponential Filter

To evaluate SM data from satellites versus *in situ*, it is necessary to consider the mismatch of representative depths

Authorized licensed use limited to: University of Virginia Libraries. Downloaded on June 11,2020 at 17:07:51 UTC from IEEE Xplore. Restrictions apply.

This article has been accepted for inclusion in a future issue of this journal. Content is final as presented, with the exception of pagination.

TABLE I

CLIMATIC CHARACTERISTICS AND SOIL PROPERTIES AT THE SEVEN SM MEASUREMENT SITES

Obs. #	1				2				3			
Location	Latitude		Longitude		Latitude		Longitude		Latitude		Longitude	
	38.8492		-75.9521		39.0231		-75.9497		38.9989		-75.8703	
Soil Moisture (0-10cm) (m^3/m^3)	min	max	std	avg	min	max	std	avg	min	max	std	avg
	0.060	0.384	0.050	0.185	0.025	0.388	0.067	0.142	0.054	0.558	0.133	0.290
Surface Temp. (˚C)	min	max	std	avg	min	max	std	avg	min	max	std	avg
	-1.400	34.900	8.722	16.118	-1.300	32.700	8.334	14.717	-1.300	34.900	7.980	13.711
Precipitation (mm/hr)	min	max	std	avg	min	max	std	avg	min	max	std	avg
	0.000	43.180	0.804	0.096	0.000	35.050	0.748	0.104	0.000	29.720	0.746	0.090
NDVI	min	max	std	avg	min	max	std	avg	min	max	std	avg
	0.378	0.885	0.130	0.572	0.404	0.852	0.127	0.600	0.416	0.844	0.104	0.638
GINI-Simpson	9-km	3-km	1-km	at site	9-km	3-km	1-km	at site	9-km	3-km	1-km	at site
	0.605	0.379	0.298	-	0.505	0.423	0.181	-	0.517	0.509	0.479	-
Land Cover	9-km	3-km	1-km	at site	9-km	3-km	1-km	at site	9-km	3-km	1-km	at site
	Cultivated Crops			Grass	Cultivated Crops			Grass	Cultivated Crops			Grass
Water Fraction	9-km	3-km	1-km	at site	9-km	3-km	1-km	at site	9-km	3-km	1-km	at site
	0.041	0	0	0	0.0033	0.00609	0	0	0.002	0	0	0
Slope (%)	0 ~ 2				5 ~ 10				0 ~ 2			
Clay (%)	10				6				16			
Silt (%)	35				25				35			
Sand (%)	55				69				49			
Soil Texture	Sand Loam				Sand Loam				Sand Loam			

Obs. #	4				5				6				7			
Location	Latitude		Longitude		Latitude		Longitude		Latitude		Longitude		Latitude		Longitude	
	38.8821		-75.8602		38.9667		-75.8492		39.1223		-75.8060		39.0743		-75.8041	
Soil Moisture (0-10cm) (m^3/m^3)	min	max	std	avg	min	max	std	avg	min	max	std	avg	min	max	std	avg
	0.035	0.426	0.068	0.209	0.035	0.306	0.052	0.143	0.063	0.435	0.072	0.211	0.025	0.422	0.081	0.216
Surface Temp. (˚C)	min	max	std	avg	min	max	std	avg	min	max	std	avg	min	max	std	avg
	-1.400	38.700	9.207	14.616	-2.500	40.100	9.518	15.898	-0.800	28.600	7.642	14.018	-2.900	40.600	9.612	12.951
Precipitation (mm/hr)	min	max	std	avg	min	max	std	avg	min	max	std	avg	min	max	std	avg
	0.000	55.120	0.809	0.102	0.000	64.520	0.836	0.113	0.000	26.920	0.724	0.102	0.000	28.190	0.694	0.069
NDVI	min	max	std	avg	min	max	std	avg	min	max	std	avg	min	max	std	avg
	0.399	0.893	0.136	0.580	0.403	0.849	0.128	0.579	0.369	0.864	0.142	0.579	0.354	0.875	0.172	0.557
GINI-Simpson	9-km	3-km	1-km	at site	9-km	3-km	1-km	at site	9-km	3-km	1-km	at site	9-km	3-km	1-km	at site
	0.638	0.516	0.200	-	0.517	0.491	0.217	-	0.684	0.625	0.574	-	0.684	0.719	0.482	-
Land Cover	9-km	3-km	1-km	at site	9-km	3-km	1-km	at site	9-km	3-km	1-km	at site	9-km	3-km	1-km	at site
	Cultivated Crops			Grass	Cultivated Crops			Bare Soil	Cultivated Crops			Grass	Cultivated Crops			Grass
Water Fraction	9-km	3-km	1-km	at site	9-km	3-km	1-km	at site	9-km	3-km	1-km	at site	9-km	3-km	1-km	at site
	0.0268	0.054	0	0	0.0015	0	0	0	0.002	0.001	0	0	0.002	0.0017	0	0
Slope (%)	2 ~ 5				2 ~ 5				2 ~ 5				0 ~ 2			
Clay (%)	9				6				8				13			
Silt (%)	31				25				17				67			
Sand (%)	60				69				75				20			
Soil Texture	Sand Loam				Sand Loam				Sand Loam				Silt Loam			

Authorized licensed use limited to: University of Virginia Libraries. Downloaded on June 11,2020 at 17:07:51 UTC from IEEE Xplore. Restrictions apply.

This article has been accepted for inclusion in a future issue of this journal. Content is final as presented, with the exception of pagination.

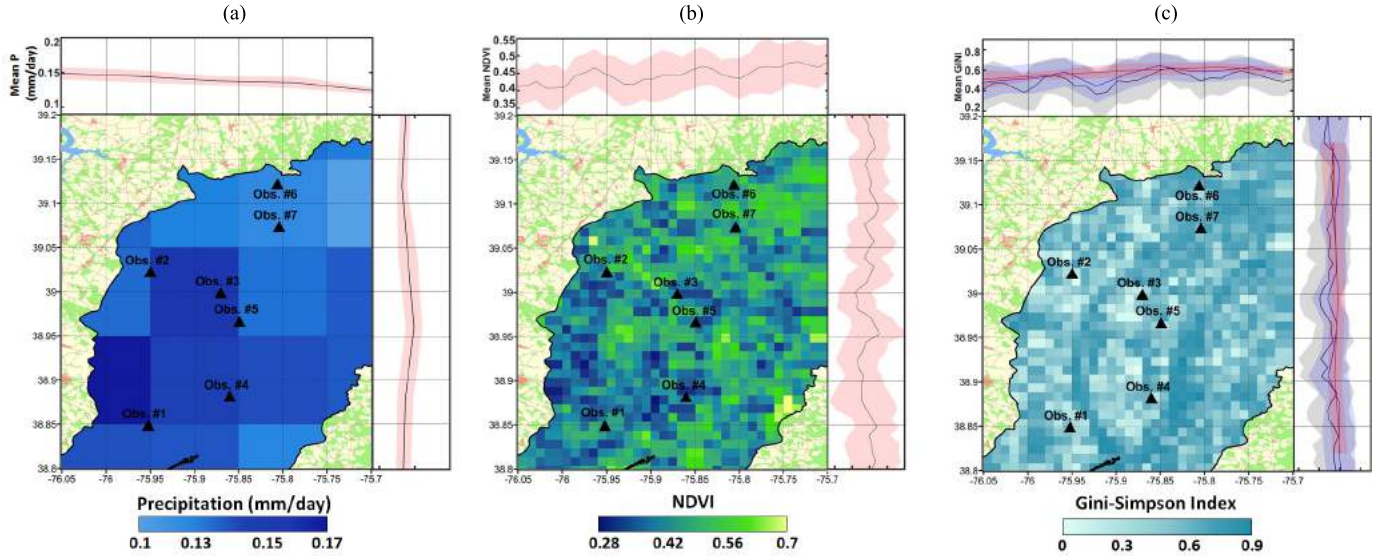

Fig. 2. Maps of (a) average precipitation from GPM, (b) average NDVI from MODIS, and (c) Gini–Simpson index. (Top right) Longitude and latitude zonal means of each variable, respectively, and the shaded region shows ±1 standard deviation. Red, black, and blue lines in the zonal mean plots in (c) indicate the average values of Gini–Simpson index for 9, 3, and 1 km, respectively.

of SM data from satellites—the T_B and radar backscatter coefficient values used to retrieve SM data originate from the topsoil layer that varies from zero to few centimeters with respect to the surface conditions, while ground-based SM data are collected from sensors installed at a fixed depth of 5 cm below the surface. An exponential filter can overcome the depth discrepancy between satellite-based SM data and ground-based measurements by estimating the average SM value over a layer in the soil profile. The satellite-based SM data, after application of the exponential filter, is called the Soil Water Index (SWI). We calculated the SWI from SMAP-9 km and SMAP/Sentinel-3- and -1-km data sets (hereafter, SMAP9SWI, SMAP3SWI, and SMAP1SWI, respectively) using the following recursive equation proposed in [73]

$$\mathrm{SMAP}x_{\mathrm{SWI}}(t_n) = \mathrm{SMAP}x_{\mathrm{SWI}}(t_{n-1}) + K_n(\mathrm{SMAP}x_{\mathrm{SWI}}(t_n) - \mathrm{SMAP}x_{\mathrm{SWI}}(t_{n-1})) \quad (1)$$

where $\mathrm{SMAP}x_{\mathrm{SWI}}(t_{n-1})$ is the estimated profile of the spatial resolution of x-km $\times x$-km SMAP SM at time $t(n-1)$, and $\mathrm{SMAP}x_{\mathrm{SWI}}(t_n)$ is the estimated profile x-km $\times x$-km SMAP SM at time t_n. The recursive form of gain K_n at time t_n is calculated as follows:

$$K_n = \frac{K_{(n-1)}}{K_{(n-1)} + e^{-\left(\frac{t_n - t_{(n-1)}}{T}\right)}} \quad \text{where } 0 < K < 1 \quad (2)$$

where T is the characteristic time length in days. In this article, we used T_{opt}, which is an optimum T value approach; T_{opt} was calculated based on the Nash–Sutcliffe score that matches the profile SM values at each ground observation. To initialize the exponential filter, $\mathrm{SMAP}x_{\mathrm{SWI}_1}$ was set to SMAP-9 km(t_1) ($x = 9$), SMAP/Sentinel-3 km ($x = 3$), and -1 km ($x = 1$), and $K1$ was set to 1, following [73].

C. Triple Collocation Analysis

Due to the multiplicative bias between satellites (or modeled) SM and *in situ* SM data, R and ubRMSE metrics can be degraded [74]. In this case, R and ubRMSE metrics could not characterize the intrinsic errors in the SMAP and SMAP/Sentinel SM data. Moreover, although the $\mathrm{SM_{REF}}$ values can be regarded as the reference values, they are not true SM values because they also include random errors and systematic errors. In this case, triple collocation (TC) metrics can be used to overcome this limitation because TC-based R^2 assumes independent error. To conduct TCA, we selected SM products with derivations as different as possible because similarly derived data sets might have partially correlated errors. We calculated the TC metric using triplets including [$\mathrm{SM_{SAT}}$, $\mathrm{SM_{MOD}}$, and $\mathrm{SM_{REF}}$]. An objective comparison of each product's error metric can be accomplished by considering a signal-to-noise ratio (SNR) [75]

$$\mathrm{SNR}_{\mathrm{SM_{SAT}}} = \frac{\mathrm{cov}(\mathrm{SM_{SAT}}, \mathrm{SM_{MOD}}) \cdot \mathrm{cov}(\mathrm{SM_{SAT}}, \mathrm{SM_{REF}})}{\mathrm{cov}(\mathrm{SM_{MOD}}, \mathrm{SM_{REF}}) \cdot \mathrm{var}(\varepsilon_{\mathrm{SAT}})} \quad (3)$$

where $\mathrm{SM_{SAT}}$ indicates SM data from SMAP or SMAP/Sentinel, $\mathrm{SM_{MOD}}$ indicates SM data from model, $\mathrm{SM_{REF}}$ indicates SM data from ground observations and var is variance of the $\mathrm{SM_{SAT}}$ error. The TC-based R^2 is different from the conventional R-values regarding its independence [76]. Because of the random errors in the reference data set, the conventional R-value can become degraded. The TC-based R^2 is calculated as follows:

$$\mathrm{TC-based}\,R^2 = \frac{1}{1 + \frac{1}{\mathrm{SNR}}}. \quad (4)$$

For further information regarding TCA, refer to [75] and [76].

Authorized licensed use limited to: University of Virginia Libraries. Downloaded on June 11,2020 at 17:07:51 UTC from IEEE Xplore. Restrictions apply.

This article has been accepted for inclusion in a future issue of this journal. Content is final as presented, with the exception of pagination.

D. CDF Matching

The CDF matching method is one of the most effective methods of removing systematic differences between two data sets using nonlinear approach [77], [78]. This approach matches the CDF of one data set (e.g., SM_{SAT} and SM_{MOD}) to the CDF of the reference data (i.e., *in situ* SM data): this method is a widely used data analysis tool using the corresponding cumulative distributions. Specifically, the CDF matching method makes it possible to remove the bias and variance error of SM_{SAT} and SM_{MOD} over the study areas. However, it is worth noting that CDF matching that allows researchers to match one set of data to the reference approach can generate artificial biases; thus, this approach has been regarded as a suboptimal method of removing the biases [74], [79], [80]. Even though the CDF matching method can be suboptimal and provides only approximations, many previous studies have proven that this method can be used to intercompare and evaluate the accuracy of the SM_{MOD} and SM_{SAT} data [80]–[82]. In this article, the CDF matching method was applied to all three SMAP-9 km (hereafter, $SMAP9_{CDF}$), SMAP/Sentinel-3 km (hereafter, $SMAP3_{CDF}$), and SMAP/Sentinel-1 km (hereafter, $SMAP1_{CDF}$).

E. Data Combining Two Different Sets of SM Data

One of the main goals of this article was to determine whether the SMAP-9 and two SMAP/Sentinel-1 SM (3 and 1 km) products contribute to improving the accuracy of the modeled SM data sets. If the SMAP data sets are capable of improving the modeled SM data, this would add great value to the use of modeled SM data in many applications. We combined three different NoahMP36 SM data products—9 km × 9 km, 3 km × 3 km, and 1 km × 1 km—using SMAP data having similar resolutions to modeled SM data from SMAP-9 km, SMAP/Sentienl-3 km, and -1 km. The final products are 9 km × 9 km spatial resolution enhanced data by NoahMP36 + SMAP (hereafter, NS9), 3 km × 3 km spatial resolution data by NoahMP36 + SMAP/Sentinel-1 (hereafter, NS3), and 1 km × 1 km spatial resolution data by NoahMP36 + SMAP/Sentinel (hereafter, NS1).

To combine the two data sets, we used the maximize-R method, which is capable of improving the temporal R-values between combined and reference data sets. This method was proposed by Kim *et al*. [83], who demonstrated that the maximize-R method is a sound method of improving the temporal R-value of certain products with respect to the reference values. Several studies have shown that the combined data produced by the maximize-R method are generally superior to the individual products of various hydrological variables, including SM and ET, obtained from satellite observations [84], [85].

The combined SM data (i.e., NS9, NS3, and NS1) were calculated by applying a weighting factor (w) with a normalized range of 0–1 as follows:

$$SM_{NSx} = w \times SM_{MOD} + (1 - w) \times SM_{SAT} \quad (x = 9, 3, \text{ or } 1) \tag{5}$$

where SM_{NSx} represents the combined SM data having a spatial resolution of x (e.g., 9, 3, or 1 km), SM_{MOD} represents the NoahMP36 SM data having an x-km resolution, and SM_{SAT} represents the SMAP-9 km ($x = 9$) or SMAP/Sentinel-x ($x = 3$ or 1) km SM data. This combination process was performed for a given observation point where both parent products were available. If the R-value of the combined product and ground observation at a given location was less than the R-value of a single parent product and the ground observation, then the parent product (i.e., the original model or satellite data) with the higher R-value data was selected for the final product. The R-value between SM_{NSx} and ground observations (SM_{REF}) can be expressed as a function of w

$$R = f(w) = \frac{E\left[\left(SM_{NSx} - \mu_{SM_{NSx}}\right)\left(SM_{REF} - \mu_{SM_{REF}}\right)\right]}{\sigma_{SM_{NSx}}\sigma_{SM_{REF}}} \tag{6}$$

where μ is the mean of the combined and reference value of SM_{NSx} or SM_{REF}, and σ is the standard deviation of SM_{NSx} or SM_{REF}. Prior to combining SM_{SAT} and SM_{MOD} using (9), the systematic difference between the SM_{REF} and each parent product (i.e., SM_{SAT} and SM_{MOD}) was removed using the equation proposed in [86]: normalizing each parent product against SM_{REF}. The SM (SM_{NORM}) data normalized against the reference product was calculated from the following equation:

$$SM_{NORM} = \left(SM_{SAT(\text{or MOD})} - \mu_{SM_{SAT(\text{or MOD})}}\right) \times \frac{\sigma_{SM_{REF}}}{\sigma_{SM_{SAT}(\text{or MOD})}} + \mu_{SM_{REF}} \tag{7}$$

where μ is the mean of modeled, satellite, or *in situ* SM data, and σ is the standard deviation of modeled, satellite, or *in situ* SM data. With normalized modeled or satellite data sets, (6) was differentiated in terms of w to calculate the w value that creates the maximum R-value (correlation coefficient) between SM_{NSx} and SM_{REF}. The w value was calculated as (8), shown at the bottom of this page, where R_{XY} is the R-value between the data sets of X and Y. In addition, a numerical method was implemented if either parent product showed a negative R-value, as explained in [84].

F. Taylor Diagram

A Taylor diagram was designed to represent multiple statistics to compare different sets of data against the reference SM data (e.g., *in situ* data) on 2-D plots [87]. In this article, we calculated a normalized standard deviation (SDV): SDV indicates the ratio of SM from satellite or modeled data to ground measurement standard deviations. In the Taylor diagram, the SDV, R-value, and RMSD are demonstrated

$$w = \frac{R_{SM_{sat}\cdot SM_{ref}} - R_{SM_{sat}\cdot SM_{mod}} \times R_{SM_{mod}\cdot SM_{ref}}}{R_{SM_{mod}\cdot SM_{ref}} - R_{SM_{sat}\cdot SM_{mod}} \times R_{SM_{sat}\cdot SM_{ref}} + R_{SM_{sat}\cdot SM_{ref}} - R_{SM_{sat}\cdot SM_{mod}} \times R_{SM_{mod}\cdot SM_{ref}}} \tag{8}$$

Authorized licensed use limited to: University of Virginia Libraries. Downloaded on June 11,2020 at 17:07:51 UTC from IEEE Xplore. Restrictions apply.

This article has been accepted for inclusion in a future issue of this journal. Content is final as presented, with the exception of pagination.

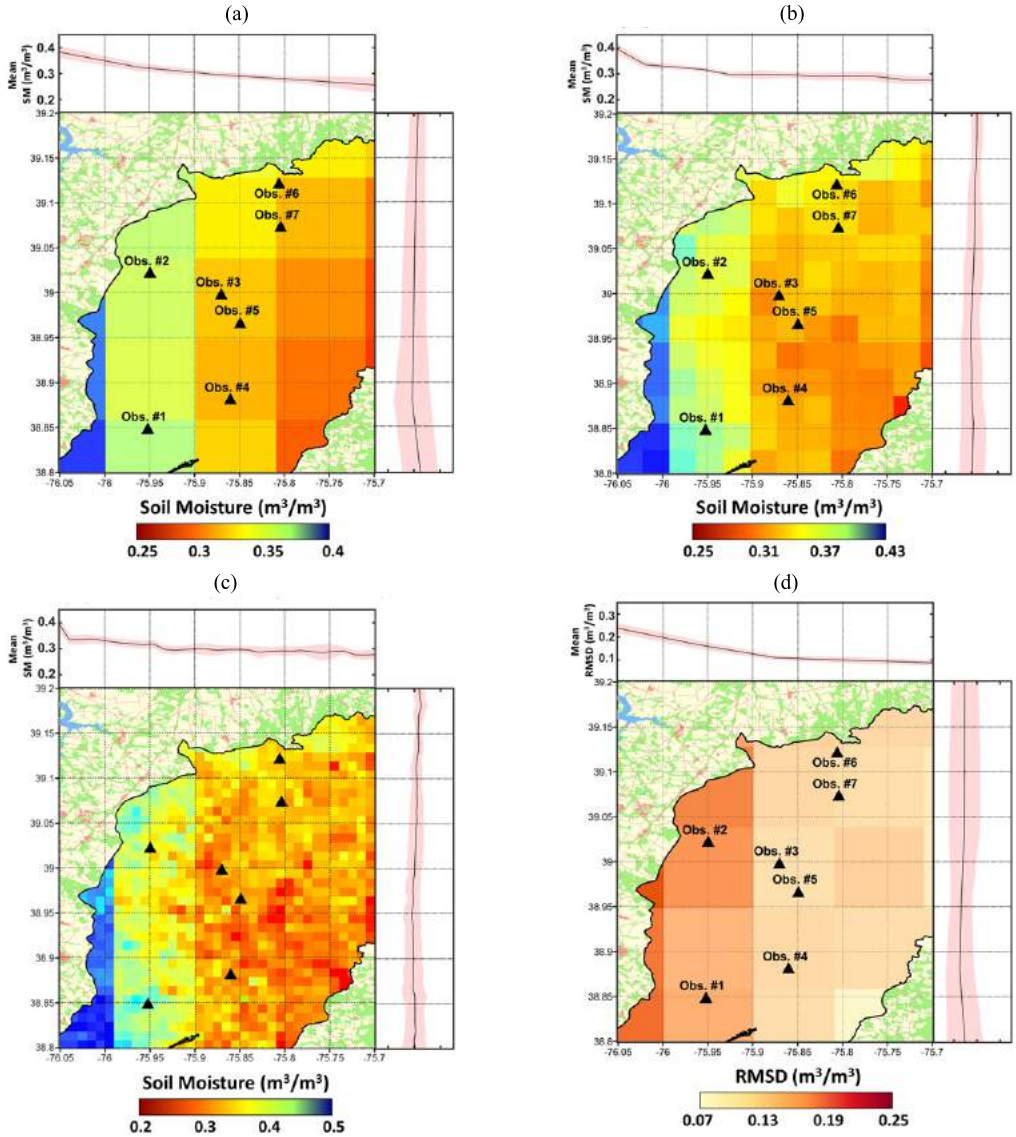

Fig. 3. Maps of average SM from (a) SMAP-9 km, (b) SMAP/Sentinel-3 km, and (c) SMAP/Sentinel-1 km. Map (d) shows the RMSD of the SMAP-9-km SM calculated using the weighted average of *in situ* SM data. The top and right panels indicate the longitude and latitude zonal means of SM for (a)–(c), and RMSD for (d), and the shaded region shows ±1 standard deviation.

simultaneously: the R-values involving ground measurements are shown as an angle in the polar plot, the SDV values are illustrated with radial distance, and the ground measurement statistics are shown as a point on the x-axis at R-value = 1 and SDV = 1. The SDV values were computed as follows:

$$\mathrm{SDV} = \frac{\sigma_{\mathrm{SM}_{\mathrm{mod(or\ \ sat\ \ or\ \ NS}x)}}}{\sigma_{\mathrm{SM}_{\mathrm{ref}}}}. \tag{9}$$

V. Results and Discussion

A. Spatial Distribution of SM From SMAP and SMAP/Sentinel

The averaged SM distributions of SMAP-9 km, SMAP/Sentinel-3 km, and -1 km are shown in Fig. 3(a)–(c). The overall spatial variations in the 3- and 1-km SMAP/Sentinel SM data showed similar spatial patterns to those of the SMAP-9 km data, but with more finely distributed SM characteristics. Approximately, 20 pixels were obtained over the study areas from the SMAP-9 km data, and 154 and 1,230 pixels were retrieved from the 3- and 1-km SMAP/Sentinel SM data, respectively. From the SMAP-9 km data [Fig. 3(a)], the diagonal gradient of SM from northwest to southeast (more longitudinal gradient than latitudinal gradient from the zonal mean plot shown on the top right of each product's average SM map) from westward to eastward is remarkable—from west to east, the topsoil tends to be drier. As the spatial resolution improves, the diagonal gradient of the SM becomes finer and noticeable. The average precipitation map from the GPM constellation satellite [Fig. 2(a)] suggests that the study area contains slightly different meteorological effects that cause different amounts of rainfall: the western part of the study area receives slightly higher amounts of precipitation than the eastern part of the study area. The general movement of storms in the temperate latitude is from

Authorized licensed use limited to: University of Virginia Libraries. Downloaded on June 11,2020 at 17:07:51 UTC from IEEE Xplore. Restrictions apply.

This article has been accepted for inclusion in a future issue of this journal. Content is final as presented, with the exception of pagination.

west to east, and the wind flow from the northwest prevails in MD, USA [88]. This climatic condition leads to the spatial gradient of the precipitation, and the SM data from SMAP are consistent with precipitation patterns. The vegetation matter indicated by NDVI was also investigated because vegetation greatly impacts SM retrievals from space. The results indicate that the study area is not densely vegetated enough to cause such an obvious diagonal SM gradient as that shown in Fig. 2(b). In Fig. 2(b), the average values of NDVI (1 km × 1 km) and the longitudinal and latitudinal average NDVI values are shown on the top left side; these values range from 0.35 to 0.7.

Land use of the study area is very homogeneous, and the land is classified mostly as croplands (Fig. 1). From these results, and the fact that our study area is very flat [35], we concluded that over the study area, SMAP and SMAP/Sentinel data can well represent the spatial patterns of SM values. However, it is worth noting that the SM values in the western part of the 9-km SMAP data seem too high when compared with the values from the eastern side of the study areas. One plausible theory for the high SM gradient pattern is a relationship between water bodies and T_B observations. As shown in Fig. 1, the western part of the study region lies adjacent to the Chesapeake Bay with an irregular coastline. The radiometer retrievals from the SMAP scan crossing the coastline could cause the change which is evident in the third Stokes parameter shown in [89]. This spike correlates closely to the area of high contrast between T_B of land and ocean at the coastline [89]; this may be an anomaly which contributes to the overestimation of SM. To analyze the spatial error patterns of the SMAP-9 km SM data, we calculated the RMSD values for each 9-km SMAP pixel using the weighted-average *in situ* data similar to [31]. We used a Voronoi diagram for weighting the *in situ* measurement in a manner similar to [31]. This diagram was selected by SMAP to find the weighting of the *in situ* observations. The Voronoi diagram, also known as a Dirichlet tessellation, is a partition of a plane into areas with respect to the distance of a given set of objects (e.g., SM *in situ* points) to each other within a bounded area. For further details about this diagram, refer to [90] and [91]. These up-scaled *in situ* SM data were then used to calculate the RMSD value for the 9-km SMAP data where *in situ* SM data do not exist. In Fig. 3(d), the result showed that pixels in the first and second columns of the SMAP-9 km data have a higher RMSD than other pixels.

However, the retrieval information in the retrieval quality flag indicates low data quality (i.e., retrieval_qaul_flag is not 0) for the first column only.

The Gini–Simpson index (i.e., the indication of heterogeneity) was also investigated because the heterogeneity of the surface could affect the SM data quality. The map of the Gini–Simpson index is shown in Fig. 2(c) (1-km EASE2 grid). The longitudinal and latitudinal average heterogeneity of the study area is shown on the top left side of Fig. 2(c). Differently colored lines and shaded areas (i.e., red and red-shaded areas, blue and blue-shaded areas, and black and gray-shaded lines) indicate the average Gini–Simpson index of SMAP and SMAP/Sentinel SM products having pixel sizes of 9, 3, and 1 km. The Gini–Simpson index values range from 0.2 to 0.7.

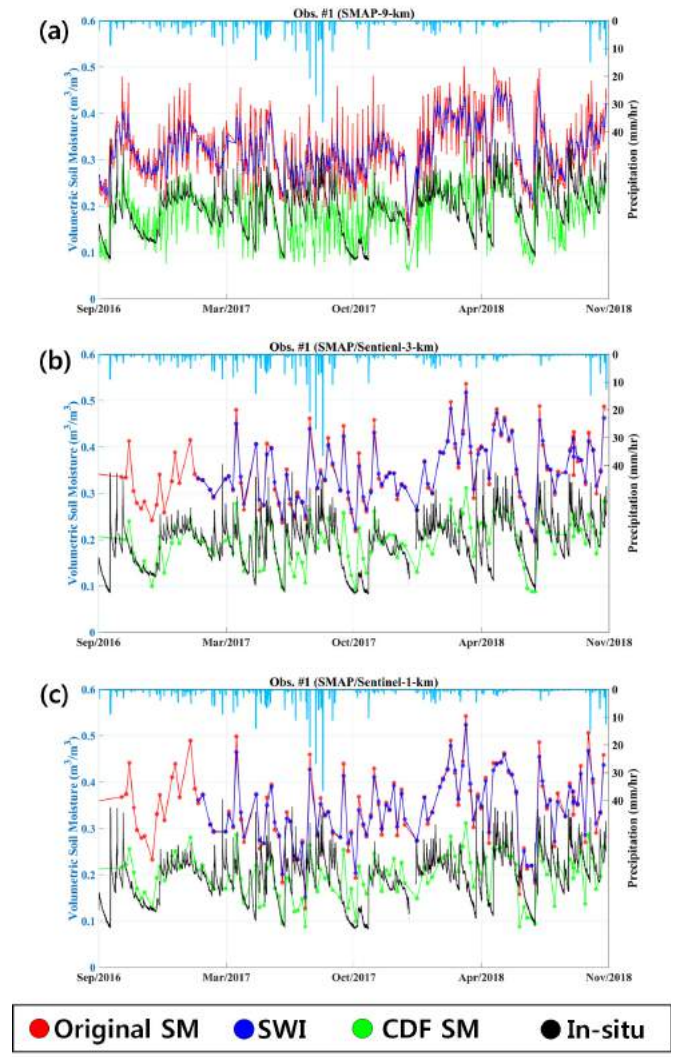

Fig. 4. Time series of SM from (a) 9-km SM products of original data (red), SWI (blue), and CDF SM (green), compared with *in situ* SM data. (b) and (c) Same information as (a) but for the SMAP/Sentinel-3- and 1-km SM data, respectively.

Over the study areas, higher spatial resolutions show slightly lower heterogeneity, but the Gini–Simpson indices for 9, 3, and 1 km do not show significantly different values because our study area consists mostly of cultivated cropland. It is worth noting that the more homogeneous the area, the more stable the SM retrieval. In addition, the higher the spatial resolution data, the higher the chance of a high fraction of water bodies in a given pixel. The pixels closest to our ground observations include barely any water bodies, as shown in Table I, row 8. This result indicates that the SMAP or SMAP/Sentinel SM data validated against *in situ* SM data (Section V-B) were not affected by water bodies that could cause errors in SM retrievals.

B. Accuracy Assessment of SMAP-9 Km and SMAP/Sentinel-3- and -1-km SM Data

The time series of SM estimates from SMAP-9 km, SMAP/Sentinel-3 km, and -1 km that include ground

Authorized licensed use limited to: University of Virginia Libraries. Downloaded on June 11,2020 at 17:07:51 UTC from IEEE Xplore. Restrictions apply.

This article has been accepted for inclusion in a future issue of this journal. Content is final as presented, with the exception of pagination.

TABLE II

VALIDATION RESULTS OF R, BIAS, AND UBRSMD VALUES FOR THE 9-km, 3-km, AND 1-km SM DATA FROM SMAP AND SMAP/SENTINEL

Original SMAP and SMAP/Sentinel SM vs. In-situ SM

	R-value			bias (m^3/m^3)			ubRMSD (m^3/m^3)		
Obs. # (nod*)	**9-km**	**3-km**	**1-km**	**9-km**	**3-km**	**1-km**	**9-km**	**3-km**	**1-km**
1 (56)	0.616	0.654	0.599	0.120	0.138	0.134	0.051	0.048	0.056
2 (54)	0.578	0.408	0.316	0.164	0.176	0.187	0.061	0.073	0.093
3 (53)	0.600	0.564	0.515	-0.025	-0.007	-0.004	0.104	0.109	0.113
4 (48)	0.782	0.746	0.649	0.042	0.048	0.052	0.041	0.042	0.055
5 (50)	0.623	0.524	0.457	0.117	0.126	0.123	0.055	0.057	0.066
6 (53)	0.718	0.668	0.625	0.064	0.079	0.081	0.057	0.061	0.068
7 (43)	0.717	0.608	0.552	0.062	0.086	0.088	0.057	0.067	0.072
Median	0.623	0.608	0.552	0.064	0.086	0.088	0.057	0.061	0.068

nod*: number of data points

observation #1 are shown in Fig. 4(a)–(c), respectively; and the results of the statistical metrics of R-value, bias, and ubRMSD are included in Table II. The data from the original SMAP, $SMAP_{SWI}$, and $SMAP_{CDF}$ for 9, 3, and 1 km are illustrated in Fig. 4. The time series results from the other observations are included in Fig. 8 in Appendix B. The most distinctive feature in SMAP/Sentinel-1A/B is the amount of data obtained during the study period. The SMAP-9 km SM data originally retrieved from the T_B values do not depend on the C-band SAR swath patterns, so it has the same spatial resolution as the SMAP-9 km SM data. Although the fine-scale 3- and 1-km SMAP/Sentinel SM data showed the potential to provide fine-resolution SM estimates by combining T_B from the SMAP radiometer and σ^0 from the Sentinel-1A/B C-band radar observations, that capability is limited due to low temporal and spatial coverage. As mentioned earlier, the temporal resolution of the SMAP/Sentinel-3- and -1-km products depends on the number of C-band SAR acquisitions from Sentinel-1A/B. The primary causes of the low spatial coverage and temporal resolutions are the relatively narrow swath of Sentinel-1A/B radar and the satellites' sun-synchronous orbit.

Specifically, the Sentinel-1 constellation's revisiting cycle of individual C-band SAR swath is approximately 12 days, and the revisiting cycle of a consecutive swath is approximately 6 days. The revisiting cycle of Sentinel-1 constellation over our study area produced pixels that varied from 6 to 14 days, while SMAP-9 km had a revisiting time of 1–2 days.

The median R-values for all networks were 0.623, 0.608, and 0.522 for SMAP-9 km, SMAP/Sentinel-3-km, and SMAP/Sentinel-1-km, respectively (R-value column in Table II). The median bias values were (0.064, 0.086, and 0.088) m^3/m^3, and the median ubRMSD values were (0.057, 0.061, and 0.068) m^3/m^3 for SMAP-9 km, SMAP/Sentiel-3 km, and SMAP/Sentinel-1 km, respectively. In terms of R-values, SMAP-9 km showed slightly better performance than the other products. In addition, the SMAP/Sentinel-3-km data had higher R-values than SMAP/Sentinel-1-km for all observations. The TC-based R-values showed similar results; for SMAP-9 km data, the TC-based R-values showed better performance than the other two products—the medians of the TC-based R-values were 0.722, 0.636, and 0.610 for SMAP-9 km, SMAP/Sentinel-3 km, and SMAP/Sentinel-1 km, respectively (Table III). The TC metrics for observation #2 with 1 km and observations #4 and #6 with 3-km and 1-km SMAP/Sentinel SM data could not be calculated due to the low number of data sets. Specifically, the number of data points for observations #2, #4, and #6 is 53, 48, and 53, respectively—numbers that are high enough for conventional metrics calculation. However, they are not a sufficient number for TCA for certain triplets. If the sample size is too small, it causes the estimated covariance matrix to be too noisy [76].

TABLE III

TCA RESULTS OF TC-BASED R-VALUES FOR THE 9-km, 3-km, AND 1-km SM DATA FROM SMAP AND SMAP/SENTINEL TC-BASED R FOR SMAP/SENTINEL SM DATA

Obs. # (nod*)	9-km	3-km	1-km
1 (55)	0.702	0.684	0.648
2 (53)	0.647	0.454	-
3 (53)	0.688	0.636	0.603
4 (48)	0.786	-	-
5 (50)	0.738	0.588	0.507
6 (53)	0.722	-	-
7 (43)	0.738	0.639	0.616
Median	0.722	0.636	0.610

nod*: number of data points

In terms of the bias of SMAP-9 km, SMAP/Sentinel-3 km, and -1 km (bias column in Table II), all SM products showed a wet bias. As we discussed in Section V-A, the coastal areas seem to contribute to the overestimation of SMAP SM data. It seems that the wet bias, which was related to the

Authorized licensed use limited to: University of Virginia Libraries. Downloaded on June 11,2020 at 17:07:51 UTC from IEEE Xplore. Restrictions apply.

This article has been accepted for inclusion in a future issue of this journal. Content is final as presented, with the exception of pagination.

TABLE IV
VALIDATION RESULTS OF R, BIAS, AND UBRSMD VALUES FOR THE $SMAP_{9SWI}$, $SMAP_{3SWI}$, AND $SMAP_{1SWI}$ DATA

SMAPxSWI vs. In-situ SM

	R-value			bias (m^3/m^3)			ubRMSD (m^3/m^3)		
Obs. # (nod*)	**9-km**	**3-km**	**1-km**	**9-km**	**3-km**	**1-km**	**9-km**	**3-km**	**1-km**
1 (55)	0.682	0.658	0.644	0.131	0.144	0.144	0.049	0.047	0.050
2 (53)	0.596	0.365	0.311	0.175	0.181	0.185	0.066	0.077	0.091
3 (53)	0.609	0.524	0.554	-0.024	-0.011	-0.011	0.099	0.108	0.105
4 (48)	0.788	0.718	0.655	0.049	0.041	0.048	0.041	0.045	0.061
5 (50)	0.572	0.314	0.264	0.115	0.120	0.118	0.060	0.065	0.076
6 (53)	0.743	0.623	0.598	0.075	0.082	0.083	0.060	0.068	0.071
7 (43)	0.690	0.495	0.431	0.070	0.083	0.081	0.060	0.073	0.079
Median	0.682	0.524	0.554	0.075	0.083	0.083	0.060	0.068	0.076

nod*: number of data points

36-km resolution of SMAP SM data, propagated to finer resolution SM retrievals because the SMAP/Sentinel-3- and -1 km data were retrieved based on the T_B values obtained from the passive radiometer onboard the SMAP. In Table X in Appendix C, it was shown that over the study areas, the SMAP L3 data (raw SM product) showed wet bias (median 0.143 m^3/m^3) when compared with seven *in situ* SM data sets. This wet bias is in contrast to the often observed dry bias over cropland [92], [93]. Vegetation canopy is known to be associated with large errors in retrieved SM, but as shown in Fig. 2(b), vegetation is not significant in this area. Furthermore, prior studies have demonstrated that SMAP shows reliable performance over cropland and moderately vegetated areas with conditions similar to those of the current study area [84]. One more possible explanation for this wet bias could be the use of the vegetation water content climatology and low clay fraction in SMAP baseline algorithm that mismatched with the actual values [94].

The median ubRMSD of SMAP-9 km, SMAP/Sentinel-3 km, and -1 km (ubRMSD column in Table II), did not meet the SMAP mission's target accuracy of 0.04 m^3/m^3. Among all products, SMAP-9 km showed the lowest ubRMSD. The pixels closest to ground observation #4 are the only area where the SMAP/Sentinel-3-km approached the target accuracy of ubRMSD. Even if we apply the exponential filter to overcome the depth discrepancy between satellite-based SM estimates and ground-observation SM data, it is difficult to see any improvement in the R-value, bias, or ubRMSD in SMAP/Sentinel-3- and -1-km products (Table IV). However, SMAP-9 km showed improvement in the R-value. The R-value (median) improved from 0.623 to 0.682. However, the profile SM of SMAP/Sentinel-3- and -1-km data was not properly estimated due to the low quantity of data, and it seems the T_{opt} value that was calculated based on the Nash–Sutcliffe score was improperly optimized (Section IV-B). Furthermore, the C-band SAR can observe shallower depths of σ^0 than SMAP's T_B observations, so using SMAP/Sentinel SM products to define their representative depth can be quite complicated.

By applying a CDF match to SMAP-9 km, SMAP/Sentinel-3 km, and -1 km, we were able to remove bias and variance errors (Table V). Even though the purpose of CDF matching is to remove systematic difference between two sets of data based on a nonlinear approach, the median R-values slightly increased from 0.623, 0.608, and 0.552 to 0.658, 0.626, and 0.570 for SMAP-9 km, SMAP/Sentinel-3 km, and -1 km, respectively. After implementation of the CDF match, the ubRMSD values for $SMAP9_{CDF}$, $SMAP3_{CDF}$, and $SMAP1_{CDF}$ were lower than both the original and the SWI data: the median ubRMSDs were 0.049, 0.053, and 0.055 m^3/m^3 for $SMAP9_{CDF}$, $SMAP3_{CDF}$, and $SMAP1_{CDF}$, respectively. The CDF match improved the accuracy of the SM data for SMAP-9 km, SMAP/Sentinel-3 km, and -1 km in terms of R-values and ubRMSDs.

In this article, we used seven *in situ* SM observations to calculate all conventional metrics (i.e., bias, RMSD, ubRMSD, and R) and TC-based R. The number of ground observation used in this article might be insufficient because the validation of the 3- and 1-km SMAP data was validated against one *in situ* station SM data. However, considering that the 9-, 3-, and 1-km data all point to a wet bias, and that the reason for the wet bias is clear, we believe the current results provide insight into the bias of SMAP data in a given area of 1-, 3-, and 9-km pixels. The p-values for testing the hypothesis also provided insight into the significance of each of these metrics. For relative metrics, we believe that conventional R [72] and TC-based R [95] metrics are better than the standard metric for SMAP SM data validation—which are pertinent and need to be reported. Chen *et al.* [95] also suggested that TC techniques offer a strategy for characterizing upscaling errors in sparse ground measurements and removing the impact of such errors from the evaluation of remotely sensed SM products. This article concluded that even in cases where ground observations provide only a single reference point within the footprint,

Authorized licensed use limited to: University of Virginia Libraries. Downloaded on June 11,2020 at 17:07:51 UTC from IEEE Xplore. Restrictions apply.

This article has been accepted for inclusion in a future issue of this journal. Content is final as presented, with the exception of pagination.

TABLE V
VALIDATION RESULTS OF R, BIAS, AND UBRSMD VALUES FOR THE $SMAP_{9CDF}$, $SMAP_{3CDF}$, AND $SMAP_{1CDF}$ DATA

SMAPxCDF vs. In-situ SM

	R-value			bias (m^3/m^3)			ubRMSD (m^3/m^3)		
Obs. # (nod*)	**9-km**	**3-km**	**1-km**	**9-km**	**3-km**	**1-km**	**9-km**	**3-km**	**1-km**
1 (55)	0.658	0.661	0.614	0	0	0	0.040	0.041	0.044
2 (53)	0.621	0.527	0.432	0	0	0	0.049	0.057	0.063
3 (53)	0.647	0.626	0.536	0	0	0	0.109	0.114	0.127
4 (48)	0.798	0.708	0.677	0	0	0	0.037	0.046	0.049
5 (50)	0.616	0.538	0.492	0	0	0	0.039	0.044	0.046
6 (53)	0.748	0.717	0.694	0	0	0	0.049	0.053	0.055
7 (43)	0.732	0.589	0.570	0	0	0	0.051	0.063	0.064
Median	0.658	0.626	0.570	0	0	0	0.049	0.053	0.055

nod*: number of data points

unbiased estimates of the correlation between the satellite product and the true footprint average can be obtained by applying the TC strategy. It is worth noting that our research site is one of the few networks near a coastline, providing a unique perspective on SM estimation from SMAP near water bodies. Furthermore, our study can have important implications on use of SMAP on coastal regions.

C. Combination of SMAP and Land Surface Model SM Products

We assumed that the combination of SMAP Enhanced and SMAP/Sentinel products would provide complementary abilities that could increase the R and lower the ubRMSD and bias values in single SM data. To combine a pair of satellite (i.e., SMAP-9 km or SMAP/Sentinel) and modeled SM products (i.e., NoahMP36), the maximize-R approach was used (Section IV-E).

The time series of SM estimates from SMAP-based, NoahMP36, and combined SM data from ground observation #1 are shown in Fig. 5(a)–(c), respectively, and the results of the statistical metrics of the R-value and ubRMSD for the comparison of the SMAP-9 km, SMAP/Sentinel-3 km and 1 km, and *in-situ* SM are included in Tables VI and VII. The original SMAP-9 km SM is illustrated with red lines; the 9-km NoahMP36 SM is indicated by blue lines; the combination of 9-km SMAP and NoahMP36 SM data, SMNS9, is shown as green lines; and the *in situ* SM data are shown as black lines [Fig. 5(a)]. Similarly, the spatial resolution of the 3- and 1-km data from SMAP/Sentinel and NoahMP36 and the combined SM time series for ground observation #1 are shown in Fig. 5(b) and (c), respectively. The time series results from the other observations are included in Fig. 9 in Appendix B. After the combination of two SM data sources, the bias values came close to zero, and the R-values and ubRMSDs were greatly improved. Figs. 5 and 9 in Appendix B clearly show that the combined SM (green lines) align well with the *in situ* SM data (black lines). Tables VI and VII show the detailed results of the statistical metrics for the 9-, 3-, and 1-km SM products obtained from SMAP (or SMAP/Sentinel-3 km and -1 km), NoahMP36, and combined SM in comparison to the *in situ* observations. The R-values and ubRMSD of the combined product (Tables VI and VII) were greatly improved in comparison to the single uses of SM product. When the SMAP-9 km and NoahMP36 data were taken alone, the median R-value versus *in situ* SM data were 0.623 and 0.777, and the ubRMSDs were (0.057 and 0.041) m^3/m^3, respectively. However, after a combination of two data sources, the median R-value increased to 0.825 and the median ubRMSD decreased to 0.034 m^3/m^3. Similarly, when the 3- and 1-km NoahMP36 data were combined with the SMAP/Sentinel-3-km and -1-km SM data, the median R-values increased significantly. Specifically, the finer resolution NoahMP36 data showed a greater R-value improvement rate than the SMAP-9 km SM data. For instance, the 3-km NoahMP36 SM R-value for observation #4 increased from 0.779 to 0.879, and the 1-km NoahMP36 SM R-value for observation #6 increased from 0.625 to 0.834—results which cannot be accomplished with coarser resolution SMAP products. These results indicate that the newly available SMAP/Sentinel data have the potential to improve the SM dynamics in modeled SM data. The ubRMSD and bias values in the combined products were greatly improved, and the combined product of satellite and modeled SM data came very close to the target accuracy of 0.04 m^3/m^3. These results are very encouraging because they show that a downscaled SMAP SM product can improve the accuracy of regional-scale SM estimates. It is noteworthy that the systematic differences between *in-situ* SM and each parent product were removed before combining the two different SM measurements from (7). Thus, the ubRMSD from a single sensor measurement decreased dramatically.

Fig. 6 presents the three Taylor diagrams illustrating a statistical comparison of data from the SMAP-9 km, 9-km NoahMP36, and SMNS9 [Fig. 6(a)]; the SMAP-9 km, 3-km NoahMP36, and SMNS3 [Fig. 6(b)], and the SMAP-9 km, 1-km NoahMP36, and SMNS1 [Fig. 6(c)] against ground observations. The temporal variability of the SM data is demonstrated by the SDV values. In all the three

Authorized licensed use limited to: University of Virginia Libraries. Downloaded on June 11,2020 at 17:07:51 UTC from IEEE Xplore. Restrictions apply.

This article has been accepted for inclusion in a future issue of this journal. Content is final as presented, with the exception of pagination.

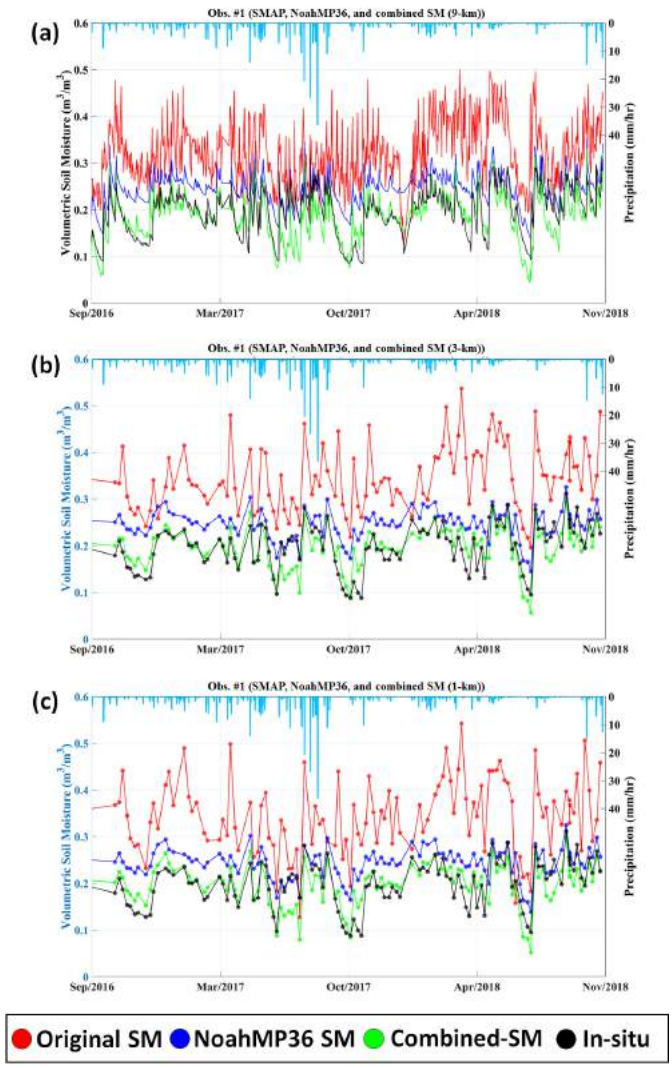

Fig. 5. Time series of SM from (a) 9-km SM products of the original data (red), NoahMP36 SM (blue), and combined SM (green), and *in situ* SM data. (b) and (c) Similar to (a) but show SMAP/Sentinel-3- and 1-km SM data, respectively.

Taylor diagrams of Fig. 6, the SDV values of the original SMAP, SMAP/Sentinel-3-, and -1-km data for the seven stations are represented by red symbols. From the R-value results, the R-values of combined products can be expected to be higher than that of the three SMAP SM products because the R-values of the NoahMP36 SM data have higher R-values than the SMAP data. All original SM products show wide scattering in the SDV, ranging from 0.49 to 1.6. The SDV value closest to 1 (red dots and lines) has the temporal variation closest to that of ground observation SM data because the SDV value represents the ratio of standard SM deviations from satellite or model products to *in situ* standard deviations. Most SMAP/Sentinel-3- and -1-km data show greater variation than *in situ* SM data. In contrast, all three resolutions of the NoahMP36 SM data demonstrate lower variation than the *in situ* SM data (blue symbols). After combination of two SM data sources, the SDV values of the combined products, SMNS9, SMNS3, and SMNS1 (represented by green symbols in Fig. 6), gather near or slightly lower than the SDV range of 1. This statistic indicates that the variability from combined products is similar to or a bit lower than that of *in situ* SM data alone. In addition, the combined products always produce a higher R-value than the individual parent products. This result emphasizes the fact that SMAP and SMAP/Sentinel products can be used to improve the temporal pattern of fine SM spatial resolutions estimated from LSMs. It is worth noting that after calculating the w factor using (8), this w factor can be used to combine two SM data sets and produce a combined product that maximizes the R-value with the reference data (*in situ* SM data). Once the w factor is determined, collecting ground SM data might be no longer required.

D. Implications

This is the first attempt to evaluate the accuracy of SMAP/Sentinel-1-km data over the coastal plain regions. Although the 1-km data had lower accuracy relative to coarser resolution data (i.e., SMAP-9 km and SMAP/Sentinel-3 km), they exhibited reliable results when combined with the NoahMP36 LSM. Demonstration of the possibility to provide high-resolution SM data has implications on water resource management. Hydrological processes vary spatiotemporally [96], impeding establishment of site-specific water management plans. As shown in Fig. 3, finer data (e.g., 1 km) better capture heterogeneity of SM over the landscape than coarser data (e.g., 9 and 3 km). Regarding that SM is a key indicator of hydrologic cycle, the 1-km SM from space data can be used as supportive data to identify specific locations experiencing water-related issues, droughts, and floods. Furthermore, high-resolution SM data can improve the credibility of process-based hydrological models that are increasingly used for water resource management [97], [98]. A common model calibration practice solely depends on observations acquired at the catchment outlet due to the lack of spatialized data, incurring predictive uncertainty [99], [100]. Inclusion of 1 km enables hydrological models to accurately depict reality by provision of additional constraints and reducing model uncertainty. However, the temporal resolution of disaggregated SM data from SMAP/Sentinel-1A/B is too coarse to be used in certain hydrological studies such as SM memory calculations [101].

This study is the first research that documents the performance of SMAP products on the "core" site within the drainage area of the Chesapeake Bay. The Chesapeake Bay is the largest and most productive estuary in the Northern America and a Ramsar wetland site of international importance [102], [103]. Albeit the Chesapeake Bay is the national and international asset, its environment is extremely deteriorated due to agricultural pollutants loads [104]. Thus, efforts to monitor hydrologic components influencing pollutant loads have been emphasized to improve the health of the Chesapeake Bay [105]. Numerous researches have been conducted on the CRW where croplands are most densely distributed within the drainage area of the Chesapeake Bay [32]. In conjunctions with the ongoing monitoring efforts [32], [106], enhanced detections of SM dynamics aid to understanding hydrologic

Authorized licensed use limited to: University of Virginia Libraries. Downloaded on June 11,2020 at 17:07:51 UTC from IEEE Xplore. Restrictions apply.

This article has been accepted for inclusion in a future issue of this journal. Content is final as presented, with the exception of pagination.

TABLE VI

VALIDATION RESULTS OF R-VALUES FOR THE 9-km, 3-km, AND 1-km RESOLUTIONS OF SMAP, NOAHMP36, AND COMBINED SM PRODUCTS

	9-km			3-km			1-km		
Obs. # (nod)	SMAP Enhanced	NoahMP36	Combined	SMAP/Sentinel	NoahMP36	Combined	SMAP/Sentinel	NoahMP36	Combined
1 (55)	0.616	0.821	0.825	0.654	0.783	0.814	0.599	0.781	0.795
2 (53)	0.578	0.798	0.810	0.377	0.778	0.781	0.316	0.799	0.799
3 (53)	0.600	0.745	0.771	0.499	0.751	0.769	0.488	0.776	0.781
4 (48)	0.782	0.727	0.853	0.746	0.779	0.879	0.649	0.779	0.838
5 (50)	0.623	0.695	0.740	0.524	0.702	0.737	0.457	0.680	0.713
6 (53)	0.718	0.791	0.854	0.668	0.770	0.850	0.625	0.707	0.834
7 (43)	0.717	0.777	0.840	0.608	0.764	0.804	0.552	0.764	0.784
Median	0.623	0.777	0.825	0.608	0.770	0.804	0.552	0.776	0.795

nod*: number of data points

TABLE VII

VALIDATION RESULTS OF UBRMSDS FOR THE 9-km, 3-km, AND 1-km RESOLUTIONS OF SMAP, NOAHMP36, AND COMBINED SM PRODUCTS

	9-km			**3-km**			**1-km**		
Obs. # (nod)	SMAP Enhanced	NoahMP36	Combined	SMAP/Sentinel	NoahMP36	Combined	SMAP/Sentinel	NoahMP36	Combined
1 (55)	0.050	0.027	0.028	0.048	0.031	0.029	0.056	0.031	0.030
2 (53)	0.061	0.035	0.034	0.073	0.037	0.036	0.093	0.037	0.037
3 (53)	0.104	0.105	0.085	0.109	0.104	0.081	0.113	0.106	0.082
4 (48)	0.041	0.041	0.031	0.042	0.041	0.029	0.055	0.041	0.033
5 (50)	0.055	0.033	0.031	0.057	0.033	0.032	0.066	0.034	0.033
6 (53)	0.057	0.045	0.036	0.061	0.049	0.037	0.068	0.053	0.039
7 (43)	0.057	0.047	0.038	0.067	0.049	0.042	0.072	0.049	0.044
Median	0.057	0.041	0.034	0.061	0.041	0.036	0.068	0.041	0.037

nod*: number of data points

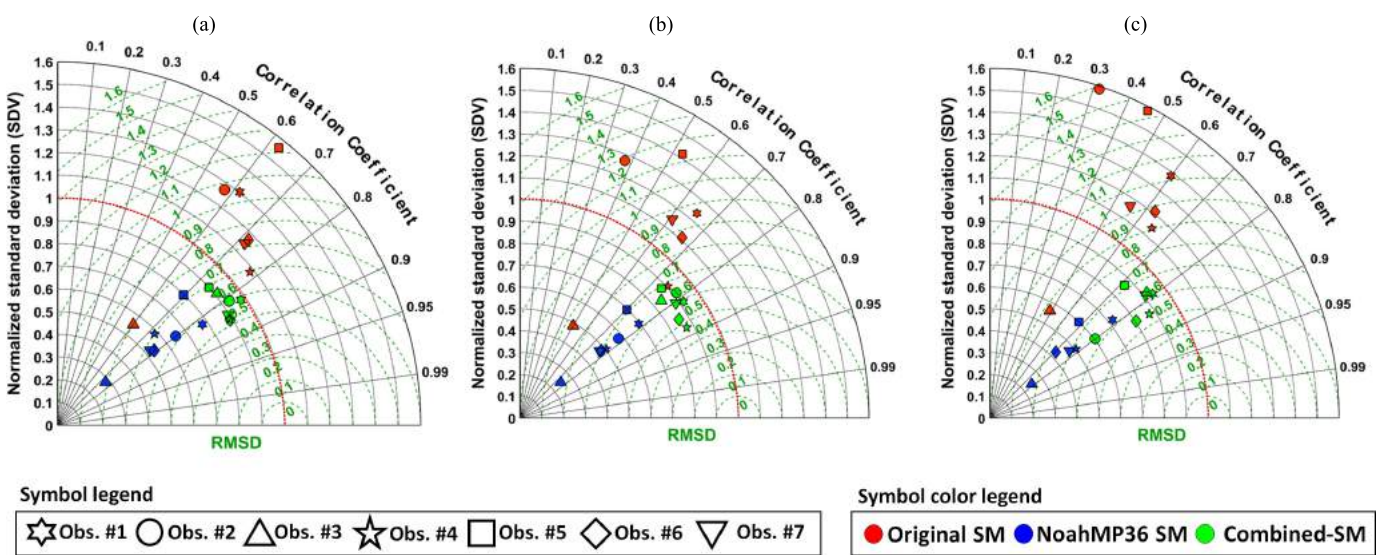

Fig. 6. Taylor diagrams show the statistical comparisons of different resolution SM products. (a) 9-, (b) 3-, and (c) 1-km SM data sets. The original SM, NoahMP36, and combined-SM products with *in situ* observations for seven different SM observations are shown with red, blue, and green symbols, respectively; each symbol indicates a different SM observation.

characteristics and associated pollutant loads in this key site. Therefore, this study can serve as one of contributing efforts to mitigate deterioration of the Bay's health.

VI. CONCLUSION

In this study, we evaluated and merged newly available high-resolution SM data (9, 3, and 1 km) retrieved from the

Authorized licensed use limited to: University of Virginia Libraries. Downloaded on June 11,2020 at 17:07:51 UTC from IEEE Xplore. Restrictions apply.

This article has been accepted for inclusion in a future issue of this journal. Content is final as presented, with the exception of pagination.

radiometer aboard SMAP and the SAR aboard Sentinel-1A/B in combination with the NoahMP36 LSM for an agricultural landscape within the Mid-Atlantic Coastal Plain. The performance of SMAP/Sentinel-3- and -1 km data is encouraging because the 3-km spatial resolution SM data can be used in many different areas that require fine-resolution SM data. The overall SM spatial pattern corresponds well to the precipitation pattern observed from GPM. An exponential filter was used to overcome the depth mismatch between satellite-based and *in situ* SM data for validation purposes, but of the three satellite observations, only the SM data from SMAP-9 km showed improvement. However, after application of the CDF matching approach, the products of all three data sources—SMAP-9 km, SMAP/Sentinel-3 km, and -1 km—improved in terms of the R-value and ubRMSD. The R-values and ubRMSD of the CDF-matched SMAP products were 0.658, 0.626, and 0.570 and 0.049, 0.053, and 0.055 m^3/m^3, respectively. By combining the SMAP data with the NoahMP36 LSM SM data, we were able to improve the overall accuracy of the SM data: the R-values for combined SM data of 9-, 3-, and 1-km resolution were 0.825, 0.804, and 0.795, and the ubRMSD values were 0.034, 0.036, and 0.037 m^3/m^3, respectively. This result shows the potential use of SMAP/Sentinel data to enhance regional-scale modeled SM data and to improve the accuracy of LSMs. In the future studies, we will assimilate the high-resolution SMAP data with various LSMs and validate the results over different core sites in CONUS and on a global scale using the International Soil Moisture Network SM data sets.

APPENDIX

A. Supplementary Information of the Study Site

TABLE VIII
LAND USE AND SOIL PROPORTIONS

Land use	Proportion (%)	HSG	Proportion (%)
Pasture	1	A	25
Open Water	1	B	34
Developed lands	6	C	40
Forest	31	D	0.0
Croplands	61	-	

Note: hydrologic soil groups (HSGs) are characterized as follows: Type A-well-drained soils with 7.6-11.4 mm/hr water infiltration rate; B - moderately well-drained soils with 3.8-7.6 mm/hr; C - moderately poorly-drained soils with 1.3-3.8 mm/hr; and D – poorly-drained soils with 0-1.3 mm/hr.

TABLE IX
DESCRIPTION OF AGGREGATED CLASSES

Aggregated class	NLCD class
Pasture	Shrub/Scrub, Herbaceuous, Hay/Pasture, and Barren Land
Open Water	Open water
Developed lands	Developed (Open Space), Developed (Medium Intensity), Developed (Low Intensity), and Developed (High Intensity),
Forest	Woody Wetlands, Emergent Herbaceuous Wetlands, Mixed Forest, Evergreen Forest, Deciduous Forest
Croplands	Cultivated Crops

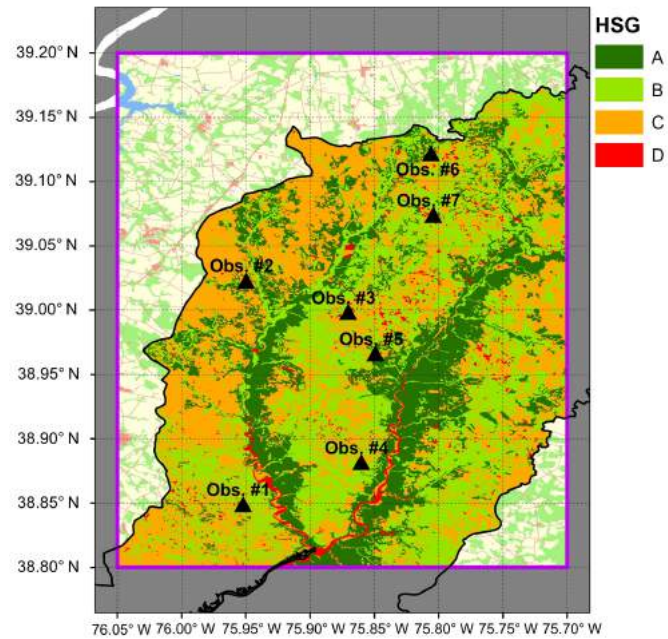

Fig. 7. Spatial distribution of hydrologic soil group.

B. Results for Obs. #2 – #7

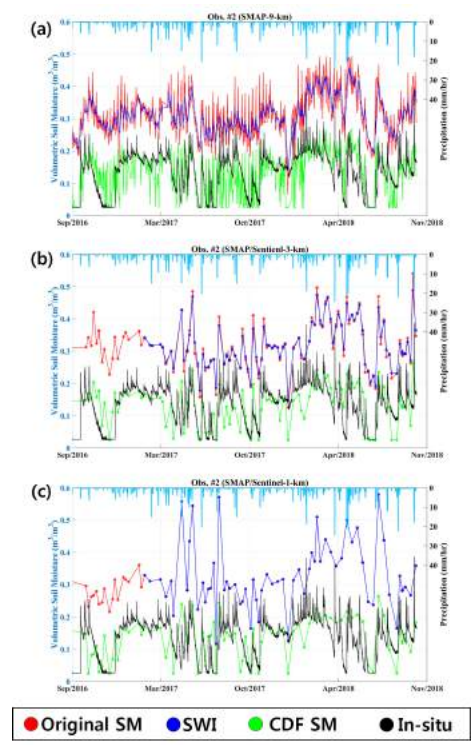

Fig. 8. Time series of SM from (a) the 9-km SM products of original data (red), SWI (blue), and CDF SM (green), compared with in-situ SM data. (b) and (c) represent the same information as (a) but for SMAP/Sentinel-3- and 1-km SM data (ground observations #2), respectively.

Authorized licensed use limited to: University of Virginia Libraries. Downloaded on June 11,2020 at 17:07:51 UTC from IEEE Xplore. Restrictions apply.

This article has been accepted for inclusion in a future issue of this journal. Content is final as presented, with the exception of pagination.

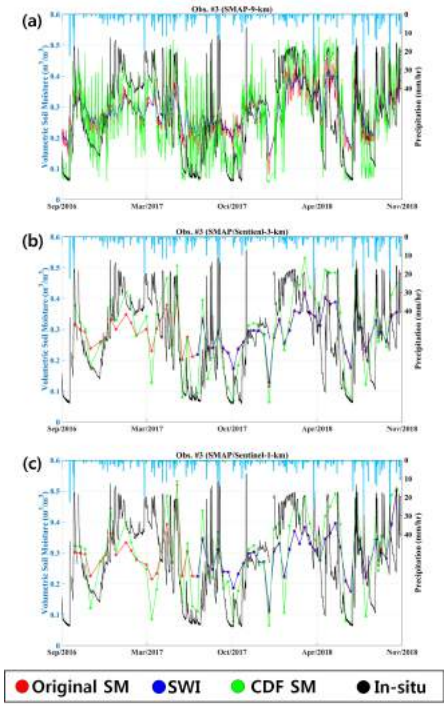

Fig. 8. *(Continued.)* Time series of SM from (a) the 9-km SM products of original data (red), SWI (blue), and CDF SM (green), compared with in-situ SM data. (b) and (c) represent the same information as (a) but for SMAP/Sentinel-3- and 1-km SM data (ground observations #3), respectively.

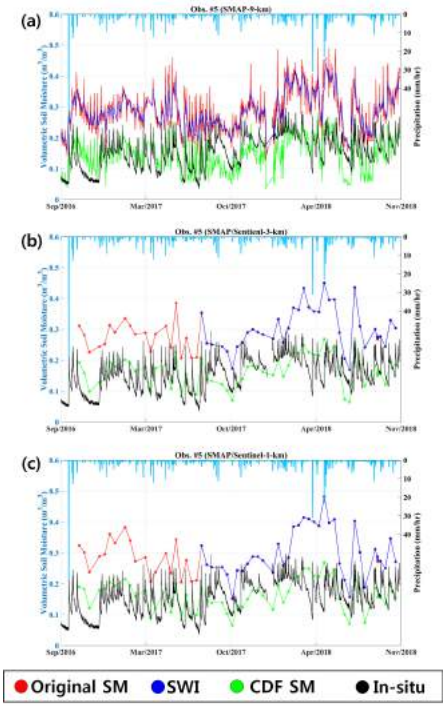

Fig. 8. *(Continued.)* Time series of SM from (a) the 9-km SM products of original data (red), SWI (blue), and CDF SM (green), compared with in-situ SM data. (b) and (c) represent the same information as (a) but for SMAP/Sentinel-3- and 1-km SM data (ground observations #5), respectively.

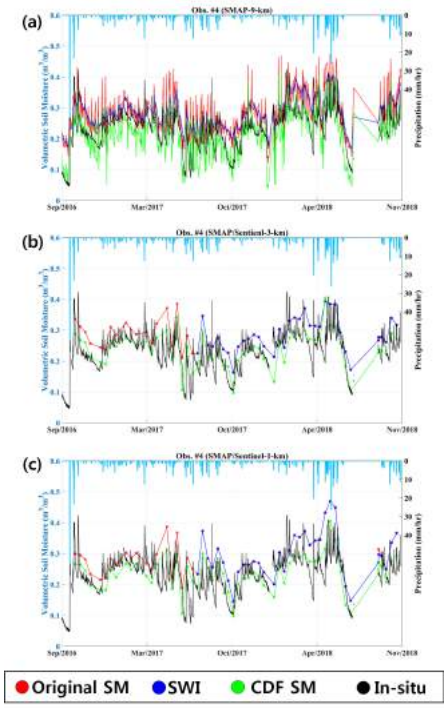

Fig. 8. *(Continued.)* Time series of SM from (a) the 9-km SM products of original data (red), SWI (blue), and CDF SM (green), compared with in-situ SM data. (b) and (c) represent the same information as (a) but for SMAP/Sentinel-3- and 1-km SM data (ground observations #4), respectively.

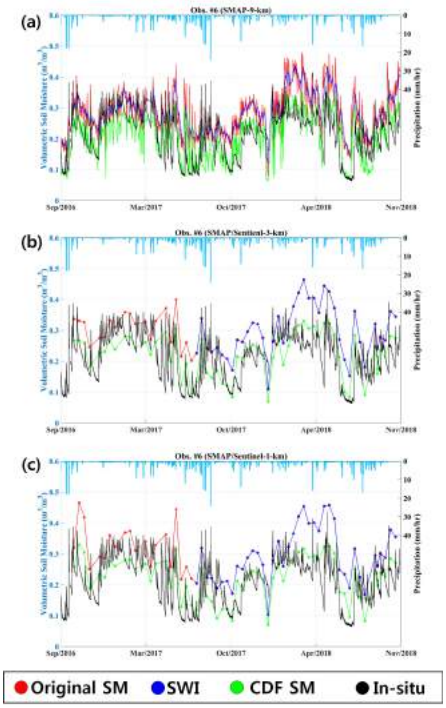

Fig. 8. *(Continued.)* Time series of SM from (a) the 9-km SM products of original data (red), SWI (blue), and CDF SM (green), compared with in-situ SM data. (b) and (c) represent the same information as (a) but for SMAP/Sentinel-3- and 1-km SM data (ground observations #6), respectively.

Authorized licensed use limited to: University of Virginia Libraries. Downloaded on June 11,2020 at 17:07:51 UTC from IEEE Xplore. Restrictions apply.

This article has been accepted for inclusion in a future issue of this journal. Content is final as presented, with the exception of pagination.

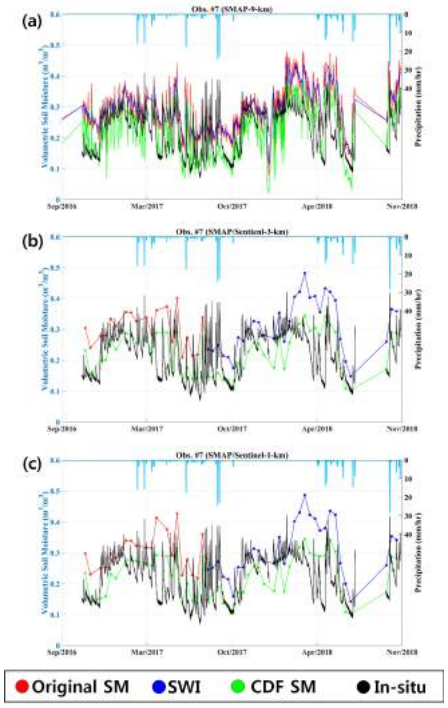

Fig. 8. *(Continued.)* Time series of SM from (a) the 9-km SM products of original data (red), SWI (blue), and CDF SM (green), compared with in-situ SM data. (b) and (c) represent the same information as (a) but for SMAP/Sentinel-3- and 1-km SM data (ground observations #7), respectively.

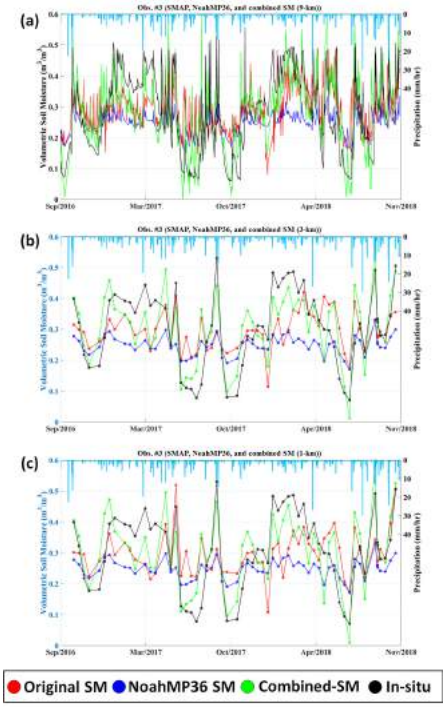

Fig. 9. *(Continued.)* Time series of SM from (a) the 9-km SM products of the original data (red), NoahMP36 SM (blue), and combined-SM (green), and in-situ SM data. (b) and (c) are similar to (a) but show SMAP/Sentinel-3- and 1-km SM data (ground observations #3), respectively.

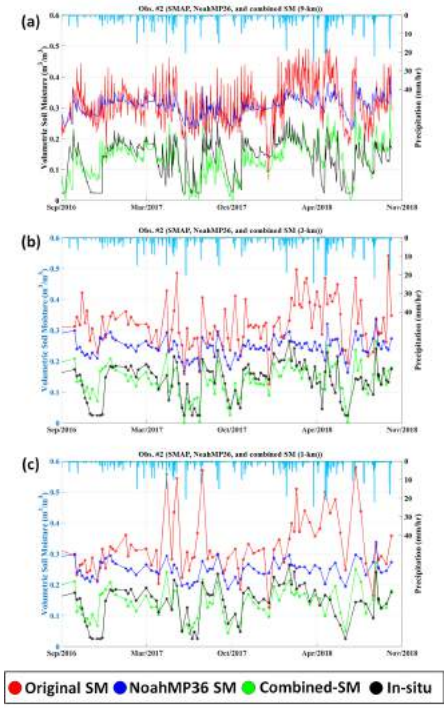

Fig. 9. Time series of SM from (a) the 9-km SM products of the original data (red), NoahMP36 SM (blue), and combined-SM (green), and in-situ SM data. (b) and (c) are similar to (a) but show SMAP/Sentinel-3- and 1-km SM data (ground observations #2), respectively.

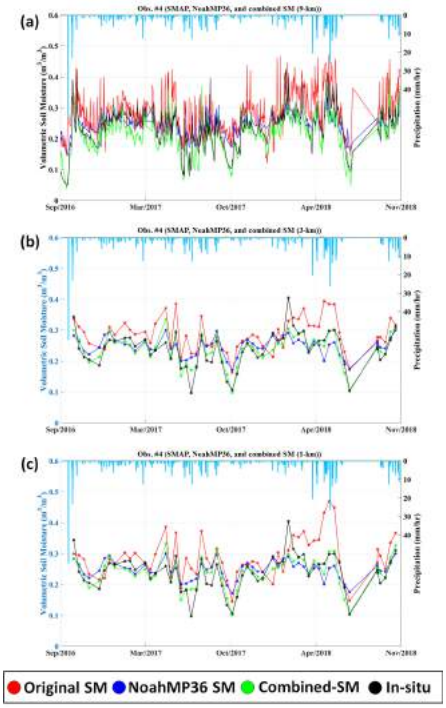

Fig. 9. *(Continued.)* Time series of SM from (a) the 9-km SM products of the original data (red), NoahMP36 SM (blue), and combined-SM (green), and in-situ SM data. (b) and (c) are similar to (a) but show SMAP/Sentinel-3- and 1-km SM data (ground observations #4), respectively.

Authorized licensed use limited to: University of Virginia Libraries. Downloaded on June 11,2020 at 17:07:51 UTC from IEEE Xplore. Restrictions apply.

This article has been accepted for inclusion in a future issue of this journal. Content is final as presented, with the exception of pagination.

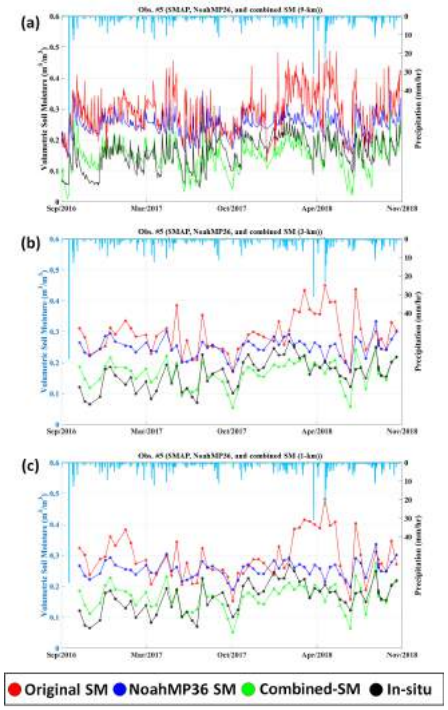

Fig. 9. *(Continued.)* Time series of SM from (a) the 9-km SM products of the original data (red), NoahMP36 SM (blue), and combined-SM (green), and in-situ SM data. (b) and (c) are similar to (a) but show SMAP/Sentinel-3- and 1-km SM data (ground observations #5), respectively.

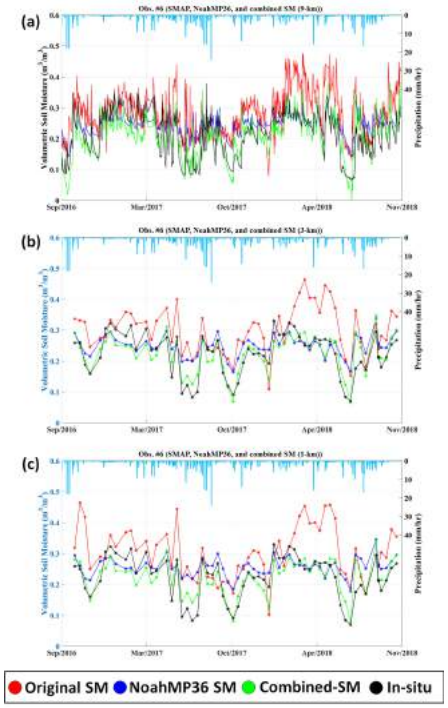

Fig. 9. *(Continued.)* Time series of SM from (a) the 9-km SM products of the original data (red), NoahMP36 SM (blue), and combined-SM (green), and in-situ SM data. (b) and (c) are similar to (a) but show SMAP/Sentinel-3- and 1-km SM data (ground observations #6), respectively.

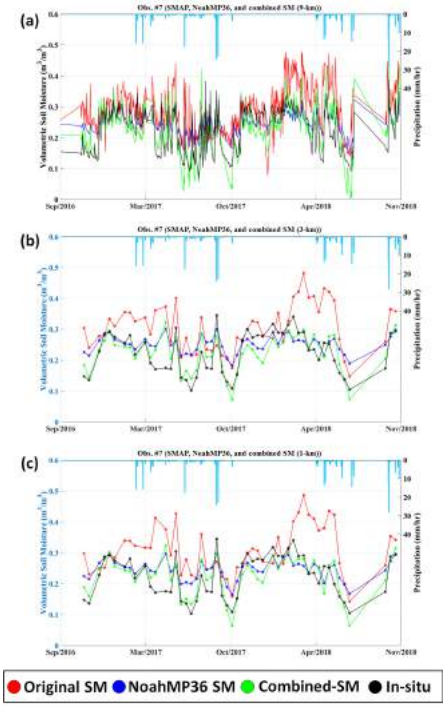

Fig. 9. *(Continued.)* Time series of SM from (a) the 9-km SM products of the original data (red), NoahMP36 SM (blue), and combined-SM (green), and in-situ SM data. (b) and (c) are similar to (a) but show SMAP/Sentinel-3- and 1-km SM data (ground observations #7), respectively.

C. Supporting Information for 36-km SM Data Validation

TABLE X
VALIDATION RESULTS OF R AND BIAS FOR THE 36-km SM DATA FROM SMAP L3

Obs.#	R-value	bias (m3/m3)
1	0.552	0.176
2	0.512	0.233
3	0.522	0.079
4	0.572	0.143
5	0.515	0.218
6	0.530	0.136
7	0.519	0.128
Median	0.522	0.143

ACKNOWLEDGMENT

The authors would like to thank the teams from NASA, USDA, NOAA, and USGS for making their data sets publicly available. They would also like to thank Research Computing at the University of Virginia, Charlottesville, VA, USA, for providing computational resources and technical support that have contributed to the results reported within this publication (https://www.rc.virginia.edu). Hyunglok Kim would like to thank Dr. Holcomb Katherine and Dr. Ruoshi Sun for their assistance. The USDA is an equal opportunity provider and employer. Any use of trade, firm, or product names is for descriptive purposes only and does not imply endorsement by the U.S. Government.

Authorized licensed use limited to: University of Virginia Libraries. Downloaded on June 11,2020 at 17:07:51 UTC from IEEE Xplore. Restrictions apply.

This article has been accepted for inclusion in a future issue of this journal. Content is final as presented, with the exception of pagination.

REFERENCES

[1] D. R. Legates *et al.*, "Soil moisture: A central and unifying theme in physical geography," *Prog. Phys. Geogr., Earth Environ.*, vol. 35, no. 1, pp. 65–86, Feb. 2011.

[2] A. M. Nahlik and M. S. Fennessy, "Carbon storage in US wetlands," *Nature Commun.*, vol. 7, no. 1, p. 13835, Dec. 2016.

[3] D. E. Fenstermacher, M. C. Rabenhorst, M. W. Lang, G. W. McCarty, and B. A. Needelman, "Carbon in natural, cultivated, and restored depressional wetlands in the Mid-Atlantic coastal plain," *J. Environ. Qual.*, vol. 45, no. 2, pp. 743–750, Mar. 2016.

[4] P. M. Lawston, J. A. Santanello, Jr., and S. V. Kumar, "Irrigation signals detected from SMAP soil moisture retrievals," *Geophys. Res. Lett.*, vol. 44, no. 23, pp. 11860–11867, Dec. 2017.

[5] R. A. M. de Jeu, W. Wagner, T. R. H. Holmes, A. J. Dolman, N. C. van de Giesen, and J. Friesen, "Global soil moisture patterns observed by space borne microwave radiometers and scatterometers," *Surv. Geophys.*, vol. 29, nos. 4–5, pp. 399–420, Oct. 2008.

[6] Y. H. Kerr *et al.*, "The SMOS soil moisture retrieval algorithm," *IEEE Trans. Geosci. Remote Sens.*, vol. 50, no. 5, pp. 1384–1403, May 2012.

[7] D. Entekhabi *et al.*, "The soil moisture active passive (SMAP) mission," *Proc. IEEE*, vol. 98, no. 5, pp. 704–716, May 2010.

[8] B. Fang and V. Lakshmi, "Soil moisture at watershed scale: Remote sensing techniques," *J. Hydrol.*, vol. 516, pp. 258–272, Aug. 2014.

[9] L. Karthikeyan, M. Pan, N. Wanders, D. N. Kumar, and E. F. Wood, "Four decades of microwave satellite soil moisture observations: Part 1. A review of retrieval algorithms," *Adv. Water Resour.*, vol. 109, pp. 106–120, Nov. 2017.

[10] E. G. Njoku, T. J. Jackson, V. Lakshmi, T. K. Chan, and S. V. Nghiem, "Soil moisture retrieval from AMSR-E," *IEEE Trans. Geosci. Remote Sens.*, vol. 41, no. 2, pp. 215–229, Feb. 2003.

[11] N. Rodriguez-Alvarez *et al.*, "Soil moisture retrieval using GNSS-R techniques: Experimental results over a bare soil field," *IEEE Trans. Geosci. Remote Sens.*, vol. 47, no. 11, pp. 3616–3624, Nov. 2009.

[12] K. Imaoka, M. Kachi, M. Kasahara, N. Ito, K. Nakagawa, and T. Oki, "Instrument performance and calibration of AMSR-E and AMSR2," *Int. Arch. Photogramm., Remote Sens. Spatial Inf. Sci.*, vol. 38, no. 8, pp. 13–18, Aug. 2010.

[13] W. A. Dorigo *et al.*, "Evaluation of the ESA CCI soil moisture product using ground-based observations," *Remote Sens. Environ.*, vol. 162, pp. 380–395, Jun. 2015.

[14] W. Wagner *et al.*, "The ASCAT soil moisture product: A review of its specifications, validation results, and emerging applications," *Meteorologische Zeitschrift*, vol. 22, no. 1, pp. 5–33, Feb. 2013.

[15] H. Kim and V. Lakshmi, "Use of cyclone global navigation satellite system (CyGNSS) observations for estimation of soil moisture," *Geophys. Res. Lett.*, vol. 45, no. 16, pp. 8272–8282, Aug. 2018.

[16] T. J. Jackson *et al.*, "Validation of advanced microwave scanning radiometer soil moisture products," *IEEE Trans. Geosci. Remote Sens.*, vol. 48, no. 12, pp. 4256–4272, Dec. 2010.

[17] R. D. Koster, S. P. P. Mahanama, B. Livneh, D. P. Lettenmaier, and R. H. Reichle, "Skill in streamflow forecasts derived from large-scale estimates of soil moisture and snow," *Nature Geosci.*, vol. 3, no. 9, pp. 613–616, Sep. 2010.

[18] J. D. Bolten, W. T. Crow, X. Zhan, T. J. Jackson, and C. A. Reynolds, "Evaluating the utility of remotely sensed soil moisture retrievals for operational agricultural drought monitoring," *IEEE J. Sel. Topics Appl. Earth Observ. Remote Sens.*, vol. 3, no. 1, pp. 57–66, Mar. 2010.

[19] L. Brocca *et al.*, "How much water is used for irrigation? A new approach exploiting coarse resolution satellite soil moisture products," *Int. J. Appl. Earth Observ. Geoinf.*, vol. 73, pp. 752–766, Dec. 2018.

[20] L. Brocca, T. Moramarco, F. Melone, W. Wagner, S. Hasenauer, and S. Hahn, "Assimilation of surface-and root-zone ASCAT soil moisture products into rainfall–runoff modeling," *IEEE Trans. Geosci. Remote Sens.*, vol. 50, no. 7, pp. 2542–2555, Jul. 2012.

[21] R. Bindlish, W. T. Crow, and T. J. Jackson, "Role of passive microwave remote sensing in improving flood forecasts," *IEEE Geosci. Remote Sens. Lett.*, vol. 6, no. 1, pp. 112–116, Jan. 2009.

[22] V. Lakshmi, T. Piechota, U. Narayan, and C. Tang, "Soil moisture as an indicator of weather extremes," *Geophys. Res. Lett.*, vol. 31, no. 11, p. l11401, Jun. 2004.

[23] R. H. Reichle, D. Entekhabi, and D. B. McLaughlin, "Downscaling of radio brightness measurements for soil moisture estimation: A four-dimensional variational data assimilation approach," *Water Resour. Res.*, vol. 37, no. 9, pp. 2353–2364, Sep. 2001.

[24] U. Narayan, V. Lakshmi, and T. J. Jackson, "High-resolution change estimation of soil moisture using L-band radiometer and radar observations made during the SMEX02 experiments," *IEEE Trans. Geosci. Remote Sens.*, vol. 44, no. 6, pp. 1545–1554, Jun. 2006.

[25] O. Merlin, J. Walker, A. Chehbouni, and Y. Kerr, "Towards deterministic downscaling of SMOS soil moisture using MODIS derived soil evaporative efficiency," *Remote Sens. Environ.*, vol. 112, no. 10, pp. 3935–3946, Oct. 2008.

[26] M. Piles *et al.*, "Downscaling SMOS-derived soil moisture using MODIS visible/infrared data," *IEEE Trans. Geosci. Remote Sens.*, vol. 49, no. 9, pp. 3156–3166, Sep. 2011.

[27] J. Peng, A. Loew, O. Merlin, and N. E. C. Verhoest, "A review of spatial downscaling of satellite remotely sensed soil moisture," *Rev. Geophys.*, vol. 55, no. 2, pp. 341–366, Jun. 2017.

[28] B. Fang, V. Lakshmi, T. J. Jackson, R. Bindlish, and A. Colliander, "Passive/active microwave soil moisture change disaggregation using SMAPVEX12 data," *J. Hydrol.*, vol. 574, pp. 1085–1098, Jul. 2019.

[29] E. Santi, S. Paloscia, S. Pettinato, L. Brocca, L. Ciabatta, and D. Entekhabi, "On the synergy of SMAP, AMSR2 and Sentinel-1 for retrieving soil moisture," *Int. J. Appl. Earth Observ. Geoinf.*, vol. 65, pp. 114–123, Mar. 2018.

[30] N. N. Das *et al.*, "High-resolution enhanced product based on SMAP active-passive approach using Sentinel 1A and 1B SAR data," in *Proc. IEEE Int. Geosci. Remote Sens. Symp. (IGARSS)*, Jul. 2017, pp. 2543–2545.

[31] A. Colliander *et al.*, "Validation of SMAP surface soil moisture products with core validation sites," *Remote Sens. Environ.*, vol. 191, pp. 215–231, Mar. 2017.

[32] G. W. McCarty *et al.*, "Water quality and conservation practice effects in the Choptank River Watershed," *J. Soil Water Conservation*, vol. 63, no. 6, pp. 461–474, Nov. 2008.

[33] L. F. Duriancik *et al.*, "The first five years of the conservation effects assessment project," *J. Soil Water Conservation*, vol. 63, no. 6, pp. 185A–197A, Nov. 2008.

[34] M. R. Walbridge and S. R. Shafer, "A long-term agro-ecosystem research (LTAR) network for agriculture," in *Proc. 4th Interagency Conf. Res. Watersheds*, Fairbanks, AK, USA, 2011, pp. 1–7.

[35] S. W. Ator, J. M. Denver, D. E. Krantz, W. Newell, and S. K. Martucci, "A surficial hydrogeologic framework for the Mid-Atlantic Coastal Plain," U.S. Dept. Interior, U.S. Geol. Surv., Reston, VA, USA, Tech. Rep. 1680, 2005.

[36] I.-Y. Yeo *et al.*, "Mapping landscape-level hydrological connectivity of headwater wetlands to downstream waters: A geospatial modeling approach—Part 1," *Sci. Total Environ.*, vol. 653, pp. 1546–1556, Feb. 2019.

[37] H. Lievens *et al.*, "Joint Sentinel-1 and SMAP data assimilation to improve soil moisture estimates," *Geophys. Res. Lett.*, vol. 44, no. 12, pp. 6145–6153, Jun. 2017.

[38] ES Agency. (2013). *Sentinel-1 User Handbook*. [Online]. Available: https://sentinel.esa.int/

[39] N. N. Das *et al.*, "The SMAP and copernicus Sentinel 1A/B microwave active-passive high resolution surface soil moisture product," *Remote Sens. Environ.*, vol. 233, Nov. 2019, Art. no. 111380.

[40] T. Jagdhuber *et al.*, "Physics-based modeling of active-passive microwave covariations for geophysical retrievals," in *Proc. IEEE Int. Geosci. Remote Sens. Symp. (IGARSS)*, Jul. 2018, pp. 250–253.

[41] T. Jagdhuber *et al.*, "Estimation of active-passive microwave covariation using SMAP and Sentinel-1 data," *Remote Sens. Environ.*, vol. 225, pp. 458–468, May 2019.

[42] R. Koster and M. Suarez, "Energy and water balance calculations in the Mosaic LSM," Nat. Aeronaut. Space Admin., Goddard Space Flight Center, Lab. Atmos., Data Assimilation Office, Greenbelt, MD, USA, Tech. Rep. 104606, 1996.

[43] X. Liang, D. P. Lettenmaier, E. F. Wood, and S. J. Burges, "A simple hydrologically based model of land surface water and energy fluxes for general circulation models," *J. Geophys. Res.*, vol. 99, no. D7, pp. 14415–14428, Jul. 1994.

[44] R. D. Koster, M. J. Suarez, A. Ducharne, M. Stieglitz, and P. Kumar, "A catchment-based approach to modeling land surface processes in a general circulation model: 1. Model structure," *J. Geophys. Res., Atmos.*, vol. 105, no. D20, pp. 24809–24822, Oct. 2000.

[45] F. Chen *et al.*, "Modeling of land surface evaporation by four schemes and comparison with FIFE observations," *J. Geophys. Res., Atmos.*, vol. 101, no. D3, pp. 7251–7268, Mar. 1996.

[46] G.-Y. Niu *et al.*, "The community Noah land surface model with multiparameterization options (Noah-MP): 1. Model description and evaluation with local-scale measurements," *J. Geophys. Res.*, vol. 116, no. D12, pp. 1–19, 2011.

Authorized licensed use limited to: University of Virginia Libraries. Downloaded on June 11,2020 at 17:07:51 UTC from IEEE Xplore. Restrictions apply.

This article has been accepted for inclusion in a future issue of this journal. Content is final as presented, with the exception of pagination.

[47] Z.-L. Yang *et al.*, "The community Noah land surface model with multiparameterization options (Noah-MP): 2. evaluation over global river basins," *J. Geophys. Res.*, vol. 116, no. D12, pp. 1–16, Jun. 2011.

[48] B. Nijssen, R. Schnur, and D. P. Lettenmaier, "Global retrospective estimation of soil moisture using the variable infiltration capacity land surface model, 1980–93," *J. Climate*, vol. 14, no. 8, pp. 1790–1808, 2001.

[49] F. Hossain and E. N. Anagnostou, "Numerical investigation of the impact of uncertainties in satellite rainfall estimation and land surface model parameters on simulation of soil moisture," *Adv. Water Resour.*, vol. 28, no. 12, pp. 1336–1350, Dec. 2005.

[50] Y. Xia *et al.*, "Comparison and assessment of three advanced land surface models in simulating terrestrial water storage components over the united states," *J. Hydrometeorol.*, vol. 18, no. 3, pp. 625–649, Mar. 2017.

[51] S. Kumar *et al.*, "Land information system: An interoperable framework for high resolution land surface modeling," *Environ. Model. Softw.*, vol. 21, no. 10, pp. 1402–1415, Oct. 2006.

[52] C. D. Peters-Lidard *et al.*, "High-performance Earth system modeling with NASA/GSFC's land information system," *Innov. Syst. Softw. Eng.*, vol. 3, no. 3, pp. 157–165, Sep. 2007.

[53] S. V. Kumar, S. Wang, D. M. Mocko, C. D. Peters-Lidard, and Y. Xia, "Similarity assessment of land surface model outputs in the North American Land Data Assimilation System," *Water Resour. Res.*, vol. 53, no. 11, pp. 8941–8965, Nov. 2017.

[54] Z. Wang, X. Zeng, and M. Decker, "Improving snow processes in the Noah land model," *J. Geophys. Res.*, vol. 115, no. D20, p. D20108, Oct. 2010.

[55] H. Wei, Y. Xia, K. E. Mitchell, and M. B. Ek, "Improvement of the Noah land surface model for warm season processes: Evaluation of water and energy flux simulation," *Hydrol. Process.*, vol. 27, no. 2, pp. 297–303, Jan. 2013.

[56] R. E. Dickinson, "Land surface processes and climate—Surface albedos and energy balance," *Adv. Geophys.*, vol. 25, pp. 305–353, Jan. 1983.

[57] G.-Y. Niu and Z.-L. Yang, "Effects of vegetation canopy processes on snow surface energy and mass balances," *J. Geophys. Res., Atmos.*, vol. 109, no. D23, pp. 1–15, Dec. 2004.

[58] Z.-L. Yang and G.-Y. Niu, "The versatile integrator of surface and atmosphere processes," *Global Planet. Change*, vol. 38, nos. 1–2, pp. 175–189, Jul. 2003.

[59] G.-Y. Niu, Z.-L. Yang, R. E. Dickinson, L. E. Gulden, and H. Su, "Development of a simple groundwater model for use in climate models and evaluation with gravity recovery and climate experiment data," *J. Geophys. Res.*, vol. 112, no. D7, pp. 1–14, Apr. 2007.

[60] Y. Xia *et al.*, "Continental-scale water and energy flux analysis and validation for the North American Land Data Assimilation System project phase 2 (NLDAS-2): 1. Intercomparison and application of model products," *J. Geophys. Res., Atmos.*, vol. 117, no. D3, pp. 1–27, Feb. 2012.

[61] W. Dorigo *et al.*, "A new international network for *in situ* soil moisture data," *Eos, Trans. Amer. Geophys. Union*, vol. 92, no. 17, pp. 141–142, 2011.

[62] M. H. Cosh *et al.*, "The soil moisture active passive Marena, Oklahoma, *in situ* sensor testbed (SMAP-MOISST): Testbed design and evaluation of *in situ* sensors," *Vadose Zone J.*, vol. 15, no. 4, Apr. 2016.

[63] J. Qi *et al.*, "Assessing the performance of a physically-based soil moisture module integrated within the soil and water assessment tool," *Environ. Model. Softw.*, vol. 109, pp. 329–341, Nov. 2018.

[64] S. Lee *et al.*, "Effects of subsurface soil characteristics on wetland-groundwater interaction in the coastal plain of the Chesapeake Bay Watershed," *Hydrol. Process.*, vol. 33, no. 2, pp. 305–315, Jan. 2019.

[65] M. C. Duniway *et al.*, "Generalizing ecological site concepts of the Colorado plateau for landscape-level applications," *Rangelands*, vol. 38, no. 6, pp. 342–349, Dec. 2016.

[66] B. Zhong and Y. J. Xu, "Scale effects of geographical soil datasets on soil carbon estimation in Louisiana, USA: A comparison of STATSGO and SSURGO," *Pedosphere*, vol. 21, no. 4, pp. 491–501, Aug. 2011.

[67] C. J. Tucker *et al.*, "An extended AVHRR 8 km NDVI dataset compatible with MODIS and SPOT vegetation NDVI data," *Int. J. Remote Sens.*, vol. 26, no. 20, pp. 4485–4498, Oct. 2005.

[68] P. S. A. Beck, C. Atzberger, K. A. Høgda, B. Johansen, and A. K. Skidmore, "Improved monitoring of vegetation dynamics at very high latitudes: A new method using MODIS NDVI," *Remote Sens. Environ.*, vol. 100, no. 3, pp. 321–334, Feb. 2006.

[69] G. J. Huffman *et al.*, "NASA global precipitation measurement (GPM) integrated multi-satellite retrievals for GPM (IMERG)," *Algorithm Theor. Basis Document*, vol. 4, p. 26, Nov. 2015.

[70] E. H. Simpson, "Measurement of diversity," *Nature*, vol. 163, no. 4148, p. 688, Apr. 1949.

[71] L. Yang *et al.*, "A new generation of the United States National land cover database: Requirements, research priorities, design, and implementation strategies," *ISPRS J. Photogramm. Remote Sens.*, vol. 146, pp. 108–123, Dec. 2018.

[72] D. Entekhabi, R. H. Reichle, R. D. Koster, and W. T. Crow, "Performance metrics for soil moisture retrievals and application requirements," *J. Hydrometeorol.*, vol. 11, no. 3, pp. 832–840, Jun. 2010.

[73] C. Albergel *et al.*, "From near-surface to root-zone soil moisture using an exponential filter: An assessment of the method based on *in-situ* observations and model simulations," *Hydrol. Earth Syst. Sci.*, vol. 12, no. 6, pp. 1323–1337, Dec. 2008.

[74] C.-H. Su, D. Ryu, W. T. Crow, and A. W. Western, "Beyond triple collocation: Applications to soil moisture monitoring," *J. Geophys. Res., Atmos.*, vol. 119, no. 11, pp. 6419–6439, Jun. 2014.

[75] A. Gruber, C.-H. Su, S. Zwieback, W. Crow, W. Dorigo, and W. Wagner, "Recent advances in (soil moisture) triple collocation analysis," *Int. J. Appl. Earth Observ. Geoinf.*, vol. 45, pp. 200–211, Mar. 2016.

[76] K. A. McColl, J. Vogelzang, A. G. Konings, D. Entekhabi, M. Piles, and A. Stoffelen, "Extended triple collocation: Estimating errors and correlation coefficients with respect to an unknown target," *Geophys. Res. Lett.*, vol. 41, no. 17, pp. 6229–6236, Sep. 2014.

[77] R. H. Reichle, "Bias reduction in short records of satellite soil moisture," *Geophys. Res. Lett.*, vol. 31, no. 19, p. L19501, Oct. 2004.

[78] Y. Y. Liu *et al.*, "Developing an improved soil moisture dataset by blending passive and active microwave satellite-based retrievals," *Hydrol. Earth Syst. Sci.*, vol. 15, no. 2, pp. 425–436, Feb. 2011.

[79] M. T. Yilmaz and W. T. Crow, "The optimality of potential rescaling approaches in land data assimilation," *J. Hydrometeorol.*, vol. 14, no. 2, pp. 650–660, Apr. 2013.

[80] E. Cho, M. Choi, and W. Wagner, "An assessment of remotely sensed surface and root zone soil moisture through active and passive sensors in northeast Asia," *Remote Sens. Environ.*, vol. 160, pp. 166–179, Apr. 2015.

[81] L. Brocca *et al.*, "Soil moisture estimation through ASCAT and AMSR-E sensors: An intercomparison and validation study across Europe," *Remote Sens. Environ.*, vol. 115, no. 12, pp. 3390–3408, Dec. 2011.

[82] C.-H. Su, D. Ryu, R. I. Young, A. W. Western, and W. Wagner, "Inter-comparison of microwave satellite soil moisture retrievals over the Murrumbidgee Basin, Southeast Australia," *Remote Sens. Environ.*, vol. 134, pp. 1–11, Jul. 2013.

[83] S. Kim, R. M. Parinussa, Y. Y. Liu, F. M. Johnson, and A. Sharma, "A framework for combining multiple soil moisture retrievals based on maximizing temporal correlation," *Geophys. Res. Lett.*, vol. 42, no. 16, pp. 6662–6670, Aug. 2015.

[84] H. Kim *et al.*, "Global-scale assessment and combination of SMAP with ASCAT (active) and AMSR2 (passive) soil moisture products," *Remote Sens. Environ.*, vol. 204, pp. 260–275, Jan. 2018.

[85] J. Baik, U. W. Liaqat, and M. Choi, "Assessment of satellite- and reanalysis-based evapotranspiration products with two blending approaches over the complex landscapes and climates of Australia," *Agricult. Forest Meteorol.*, vol. 263, pp. 388–398, Dec. 2018.

[86] C. S. Draper, J. P. Walker, P. J. Steinle, R. A. De Jeu, and T. R. Holmes, "An evaluation of AMSR-E derived soil moisture over Australia," *Remote Sens. Environ.*, vol. 113, no. 4, pp. 703–710, Apr. 2009.

[87] K. E. Taylor, "Summarizing multiple aspects of model performance in a single diagram," *J. Geophys. Res., Atmos.*, vol. 106, no. D7, pp. 7183–7192, Apr. 2001.

[88] A. M. Sexton, A. M. Sadeghi, X. Zhang, R. Srinivasan, and A. Shirmohammadi, "Using NEXRAD and rain gauge precipitation data for hydrologic calibration of SWAT in a /northeastern Watershed," *Trans. ASABE*, vol. 53, no. 5, pp. 1501–1510, 2010.

[89] D. M. Le Vine and S. Abraham, "Faraday rotation and the SMAP radiometer," in *Proc. 14th Spec. Meeting Microw. Radiometry Remote Sens. Environ. (MicroRad)*, Apr. 2016, pp. 25–26.

[90] G. Voronoi, "Nouvelles applications des paramètres continus à la théorie des formes quadratiques. Premier mémoire. Sur quelques propriétés des formes quadratiques positives parfaites," *J. für die reine und angewandte Mathematik*, vol. 133, pp. 97–102, Jan. 1908.

[91] S. L. Dingman, *Physical Hydrology*. Long Grove, IL, USA: Waveland Press, 2015.

[92] W. J. Rondinelli *et al.*, "Different rates of soil drying after rainfall are observed by the SMOS satellite and the South Fork *in situ* soil moisture network," *J. Hydrometeorol.*, vol. 16, no. 2, pp. 889–903, Apr. 2015.

Authorized licensed use limited to: University of Virginia Libraries. Downloaded on June 11,2020 at 17:07:51 UTC from IEEE Xplore. Restrictions apply.

This article has been accepted for inclusion in a future issue of this journal. Content is final as presented, with the exception of pagination.

[93] V. A. Walker, B. K. Hornbuckle, and M. H. Cosh, "A five-year evaluation of SMOS level 2 soil moisture in the corn belt of the United States," *IEEE J. Sel. Topics Appl. Earth Observ. Remote Sens.*, vol. 11, no. 12, pp. 4664–4675, Dec. 2018.

[94] G. Singh *et al.*, "Validation of SMAP soil moisture products using ground-based observations for the paddy dominated tropical region of India," *IEEE Trans. Geosci. Remote Sens.*, vol. 57, no. 11, pp. 8479–8491, Nov. 2019.

[95] F. Chen *et al.*, "Application of triple collocation in ground-based validation of soil moisture active/passive (SMAP) level 2 data products," *IEEE J. Sel. Topics Appl. Earth Observ. Remote Sens.*, vol. 10, no. 2, pp. 489–502, Feb. 2017.

[96] B. Sivakumar and V. P. Singh, "Hydrologic system complexity and nonlinear dynamic concepts for a catchment classification framework," *Hydrol. Earth Syst. Sci.*, vol. 16, no. 11, pp. 4119–4131, 2012.

[97] R. Muñoz-Carpena, G. Vellidis, A. Shirmohammadi, and W. W. Wallender, "Evaluation of modeling tools for TMDL development and implementation," *Trans. ASABE*, vol. 49, no. 4, pp. 961–965, 2006.

[98] P. W. Gassman, A. M. Sadeghi, and R. Srinivasan, "Applications of the SWAT model special section: Overview and insights," *J. Environ. Qual.*, vol. 43, no. 1, pp. 1–8, Jan. 2014.

[99] J. Seibert and J. J. McDonnell, "On the dialog between experimentalist and modeler in catchment hydrology: Use of soft data for multicriteria model calibration," *Water Resour. Res.*, vol. 38, no. 11, p. 1241, Nov. 2002.

[100] K. Beven, "A manifesto for the equifinality thesis," *J. Hydrol.*, vol. 320, nos. 1–2, pp. 18–36, Mar. 2006.

[101] H. Kim and V. Lakshmi, "Global dynamics of stored precipitation water in the topsoil layer from satellite and reanalysis data," *Water Resour. Res.*, vol. 55, no. 4, pp. 3328–3346, Apr. 2019.

[102] *Chesapeake Executive Council, Chesapeake 2000 Agreement*, Chesapeake Bay Program, Annapolis, MD, USA, 2000.

[103] R. Gardner and N. Davidson, "The Ramsar convention," in *Wetlands*. Dordrecht, The Netherlands: Springer, 2011, pp. 189–203.

[104] *National Research Council, Achieving Nutrient and Sediment Reduction Goals in the Chesapeake Bay: An Evaluation of Program Strategies and Implementation*, Nat. Academies Press, Washington, DC, USA, 2011.

[105] *Executive Order 13508, Fiscal Year 2011 Action Plan, Strategy for Protecting and Restoring the Chesapeake Bay Watershed, Federal Leadership Committee for the Chesapeake Bay*, Chesapeake Bay Program, Annapolis, MD, USA, 2011.

[106] L. Sun *et al.*, "Investigating water use over the Choptank River Watershed using a multisatellite data fusion approach," *Water Resour. Res.*, vol. 53, no. 7, pp. 5298–5319, Jul. 2017.

Hyunglok Kim received the B.S. degree in civil and environmental engineering from Hanyang University, Seoul, South Korea, in 2012, and the M.S. degree in water resources from Sungkyunkwan University, Suwon, South Korea, in 2016. He is pursuing the Ph.D. degree in civil and environmental engineering with the University of Virginia, Charlottesville, VA, USA.

He is a Future Investigators in NASA Earth and Space Science and Technology (FINESST' 2019) with his project titled "Diurnal Soil Moisture Using Satellite Observations and Data Assimilation." His research interests include studies of active and passive microwave remote sensing of soil moisture, land surface hydrology, and data assimilation.

Sangchul Lee received the B.S. and M.S. degrees in environmental science and ecological engineering from Korea University, Seoul, South Korea, in 2007 and 2011, respectively, and the Ph.D. degree in geographical sciences from the University of Maryland, College Park, MD, USA, in 2017.

He is with the University of Maryland, and also with the U.S. Department of Agriculture—Agricultural Research Service, Hydrology and Remote Sensing Laboratory, Beltsville, MD. His research interest includes remote sensing data and hydrological modeling applications in landscape hydrology.

Michael H. Cosh (Senior Member, IEEE) received the Ph.D. degree in civil and environmental engineering from Cornell University, Ithaca, NY, USA, in 2002.

He is a Research Hydrologist with the U.S. Department of Agriculture, Agricultural Research Service, Hydrology and Remote Sensing Laboratory, Beltsville, MD, USA. His research interest includes the monitoring of soil moisture from both *in situ* resources and satellite products.

Venkataraman Lakshmi received the bachelor's degree in civil engineering from the University of Roorkee, Roorkee, India, in 1987, and the Doctorate degree in civil and environmental engineering from Princeton University, Princeton, NJ, USA, in 1996.

From 1996 to 1999, he was a Research Scientist with the Laboratory for the Atmospheres, NASA Goddard Space Flight Center, Greenbelt, MD, USA. From 1999 to 2018, he was the Carolina Trustee Professor and the former Chair of the Department of Earth and Ocean Sciences, University of South Carolina, Columbia, SC, USA. He is currently a Professor with the Department of Engineering Systems and the Environment, University of Virginia, Charlottesville, VA, USA. He was a Cox Visiting Professor with Stanford University, from 2006 to 2007 and 2015 to 2016, and the Program Director for Hydrologic Sciences with the National Science Foundation from 2017 to 2018. He has more than 120 peer-reviewed articles and 400 presentations and thesis supervisor for 25 graduate students. His areas of research interest are catchment hydrology, satellite data validation and assimilation, field experiments, land–atmosphere interactions, satellite data downscaling, vadose zone, and water resources.

Dr. Lakshmi is a fellow of the American Society of Civil Engineers (ASCE) and the Geological Society of America (GSA). He is serving as a member for the Water Science and Technology Board, National Academy of Sciences. He has served on the National Academies Panel for the Decadal Survey of Earth Observations from Space (NASA) and as the Chair of the Planning Committee for Groundwater Recharge and Flow: Approaches and Challenges for Monitoring and Modeling Using Remotely Sensed Data (NGA).

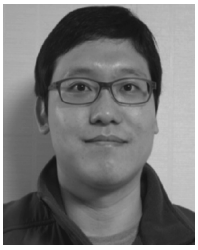

Yonghwan Kwon received the B.S.A. degree in environmental education and the M.C.P. degree in environmental management from Seoul National University, Seoul, South Korea, in 2004 and 2009, respectively, and the Ph.D. degree in geological sciences from The University of Texas at Austin, Austin, TX, USA, in 2016.

He is with the NASA Land Information System (LIS) Team, Hydrological Sciences Laboratory, NASA Goddard Space Flight Center, Greenbelt, MD, USA. His research interests include land surface hydrological modeling, snow and soil moisture data assimilation, microwave radiative transfer in snowpacks, hydrological applications of machine-learning methods, and land–atmosphere interactions.

Gregory W. McCarty received the Ph.D. degree in agronomy from Iowa State University, Ames, IA, USA, in 1989.

He is with the U.S. Department of Agriculture—Agricultural Research Service, Hydrology and Remote Sensing Laboratory, Beltsville, MD, USA. His research interests include analysis of ecosystem services and biogeochemical processes in agricultural landscapes using *in situ* observations, and remote sensing data and modeling.

Authorized licensed use limited to: University of Virginia Libraries. Downloaded on June 11,2020 at 17:07:51 UTC from IEEE Xplore. Restrictions apply.